

Computational Modelling of a Nanowire

A Project Report

submitted by

ANKIT SHUKLA

*in partial fulfilment of the requirements
for the award of the degree of*

BACHELOR OF TECHNOLOGY

and

MASTER OF TECHNOLOGY



**DEPARTMENT OF ELECTRICAL ENGINEERING
INDIAN INSTITUTE OF TECHNOLOGY MADRAS.**

MAY 2017

THESIS CERTIFICATE

This is to certify that the thesis titled **Computational Modelling of a Nanowire**, submitted by **Ankit Shukla**, to the Indian Institute of Technology, Madras, for the award of the degree of **Bachelor of Technology and Master of Technology**, is a bona fide record of the research work done by him under our supervision. The contents of this thesis, in full or in parts, have not been submitted to any other Institute or University for the award of any degree or diploma.

Prof. 1
Research Guide
Dr. Anjan Chakravorty
Dept. of Electrical Engineering
IIT-Madras, 600 036

Place: Chennai

Date: 18th May 2017

ACKNOWLEDGEMENTS

I would like to express my sincere gratitude to my advisor, Dr. Anjan Chakravorty for all the guidance, help, support and freedom that he rendered during the course of my work. His constant encouragement was always a source of motivation and played a crucial role in the completion of this work.

I sincerely thank Dr. Deleep R. Nair for providing insightful comments at various stages of my research work. I would like to take this opportunity to thank all my professors here at IIT Madras especially Prof. S Karmalkar, Prof. David Koilpillai, Dr. Nagendra Krishnapura, and Prof. Amitava Dasgupta for their fantastic lectures and teaching style.

I'm extremely thankful to all my lab mates from ESB001 especially Nidhin and Dibakar for all their valuable time that they spent discussing the issues faced by me during the course of the last one year.

I'm also extremely thankful to my mother, father, brother and other relatives for their constant love, support and understanding.

Last five years at IIT Madras have been wonderful mostly due to my friends especially Akash, Akshat, Ayush, Deshmkuh, Sant, Atharv, Shubham, Amal, Rahul, Adit, Aroon and Abhinash. I would like to thank them for bearing up with me and for all the brilliant memories that I'll cherish throughout my life.

Lastly, I thank IIT Madras, the Government of India and the Alumni of IITM for the facilities that they provide us in our hostels and labs.

ABSTRACT

KEYWORDS: NEGF; mode-space; semi-classical; quantum; Fourier's Law.

Conventional Silicon Metal Oxide Field Effect Transistors(MOSFETs) have reached their scaling limits. For more than a decade now researchers in both industry and academia have been working on alternative materials like high-K/metal gate combination, compound semiconductors, viz. GaAs, GaN as substrate. As an alternative substrate research groups are also looking at 2D material like Graphene, XS_2 .

There has been a simultaneous effort to explore alternative architecture like the Fin-FETs and other multiple gate transistors like Silicon Nanowire Transistor(SNWT). Theoretically SNWT has been explored extensively in the last decade because of its better control over the channel. The objective of this thesis is to present the physics that governs the functioning of a SNWT, through numerical simulations. A three dimensional self consistent SNWT simulator has been developed based on the effective mass approximation to study different transport mechanisms.

TABLE OF CONTENTS

ABSTRACT	ii
LIST OF FIGURES	vi
ABBREVIATIONS	vii
1 INTRODUCTION	1
1.1 Background	1
1.2 Device, its Physics and the simulation technique	2
1.2.1 The Device	2
1.2.2 Physics involved	3
1.2.3 Self-Consistent simulation scheme	4
1.3 Overview of the thesis	4
2 Quantum effects and ballistic transport	6
2.1 Poisson’s Equation	6
2.1.1 Boundary Conditions	7
2.1.2 Solving the equation	9
2.2 Schrodinger’s Equation	10
2.2.1 Mode Space Approach	11
2.2.2 Implementation	13
2.3 Transport	13
2.3.1 Semi-classical Ballistic Transport	14
2.3.2 Quantum Ballistic Transport	17
2.4 Bench marking, Comparisons and Validation	23
2.4.1 Bench marking	23
2.4.2 Semi-classical and Quantum ballistic transport	24
3 Diffusive Transport	29
3.1 Drift-Diffusion Transport	29

3.2	Quantum Dissipative Transport	34
3.3	Results and Discussions	39
4	Self Heating Effects in a Silicon Nanowire	43
4.1	Fourier's Law	44
4.2	Thermal Conductivity	46
4.3	Results and discussion	46
5	CONCLUSION	50
5.1	Summary	50
5.2	Scope for future work	51

LIST OF FIGURES

1.1	Transistor Architectures for present and future generations	2
1.2	Design of Silicon Nanowire Transistor	3
1.3	Flow chart of the self-consistent simulation scheme followed in the simulator	4
2.1	Grid structure at every x. 2D Schrodinger's equation is solved on this grid using FDM	13
2.2	Charge transport in the top of the barrier model	14
2.3	I_D vs. V_D for a 10 nm channel length	17
2.4	First subband variation vs. V_D for a 10nm channel length	18
2.5	Electron charge concentration variation vs. V_D for a 10nm channel length	18
2.6	qbte:Current vs. Gate voltage for a 10nm device for quantum ballistic model	23
2.7	qbte:First subband variation vs. V_G for a 10nm channel length	23
2.8	qbte:Electron charge concentration variation vs. V_G for a 10nm channel length	24
2.9	Current voltage curve for a 3nm x 3nm Silicon body cross-section and 15 nm channel length	24
2.10	Current voltage curve for a 3nm x 3nm Silicon body cross-section and 10 nm channel length	25
2.11	Current voltage curve for a 3nm x 3nm Silicon body cross-section and 15 nm channel length	25
2.12	Current voltage curve for a 3nm x 3nm Silicon body cross-section and 10 nm channel length	26
2.13	Current vs drain voltage curve of a 10 nm channel length for clbte and qbte	26
2.14	Current vs drain voltage curve of a 15 nm channel length for clbte and qbte	26
2.15	Current vs drain voltage curve of a 5 nm channel length for clbte and qbte	27
2.16	Current vs gate voltage curve of a 15 nm channel length for clbte and qbte	27

2.17	Current vs gate voltage curve of a 10 nm channel length for clbte and qbte	27
2.18	Current vs gate voltage curve of a 5 nm channel length for clbte and qbte	28
3.1	Representation of Buttiker's probes attached to a mode. The arrows show current flowing in and out of the probe	36
3.2	Current vs drain voltage curve of a 15 nm channel length for clbte and dd	40
3.3	Current vs drain voltage curve of a 10 nm channel length for clbte and dd	40
3.4	Current vs drain voltage curve of a 15 nm channel length for qbte and qdte	41
3.5	Current vs drain voltage curve of a 10 nm channel length for qbte and qdte	41
3.6	Current vs drain voltage curve of a 5 nm channel length for qbte and qdte	41
3.7	Current vs gate voltage curve of a 15 nm channel length for qbte and qdte	42
3.8	Current vs gate voltage curve of a 5 nm channel length for qbte and qdte	42
4.1	Current vs drain voltage curve of a 15 nm channel length for qbte and qdte	47
4.2	Current vs drain voltage curve of a 10 nm channel length for qbte and qdte	47
4.3	Current vs drain voltage curve of a 5 nm channel length for qbte and qdte	47
4.4	Current vs gate voltage curve of a 5 nm channel length for qbte and qdte	48
4.5	Temperature variation along the transport direction for different V_D when source, drain and gate are all heat sinks	48
4.6	Temperature variation along the transport direction for different V_D when only source and drain are heat sinks	49

ABBREVIATIONS

CLBTE	Classical Ballistic Transport Equation
QBTE	Quantum Ballistic Transport Equation
QDTE	Quantum Dissipative Transport Equation
DD	Drift Diffusion
NEGF	Non Equilibrium Green Function
BTE	Boltzmann Transport Equation

CHAPTER 1

INTRODUCTION

1.1 Background

Since the invention of MOS transistors semiconductor industry has grown rapidly and led to the Information Technology revolution which has changed our lives and the whole world. The main reason behind this is the increase in the speed of the transistors and hence the Integrated Circuits(ICs).

The above mentioned speed gain is basically achieved by scaling down the size of the transistors proportionately [1]. When transistors are scaled down, the charge carriers need lesser time to go from source to drain, resulting in an increase in the switching speed. They also encounter lower scattering as compared to long channel devices. Present day SOI devices face even lower scattering because of volume inversion [2]. Gordon Moore had predicted that the number of transistors on an integrated circuit chip would double after every two years and device engineers have explored alternative materials and alternative architecture to make sure that the scaling trend continues. This has resulted in packaging more transistors per unit area of a die which leads to faster communication between transistors. Figure 1.1 (courtesy[3]) shows various architectures that are being considered to continue Moore's law.

Scaling, however, comes at the cost of short channel effects like threshold voltage(V_T) roll-off and Drain Induced Barrier Lowering(DIBL)[4]. Basically, the reduced channel length decreases the control of gate over the channel and the source-drain electric field becomes significant when compared to the transverse electric field. SOI MOSFETs are a good alternative to bulk transistors, however, in nanoscale regime the scaling capability and hence the performance of both planar bulk or SOI MOSFETs are limited due to increased leakage and SCEs. Low mobility of Silicon when compared to other materials is another limiting factor.

In order to overcome the above mentioned limitations, researchers have used a high-K dielectric/metal gate combination to reduce leakage current; different channel mate-

materials like Si on Ge to increase mobility and other 2D materials like graphene. Several research groups have, however, shown confidence in the existing Silicon technology and developed alternative architecture like Double Gate Field Effect Transistors(DGFETs), FinFETs(a triple gate non-planar FET), Gate All Around Field Effect Transistors(GAAFETs).

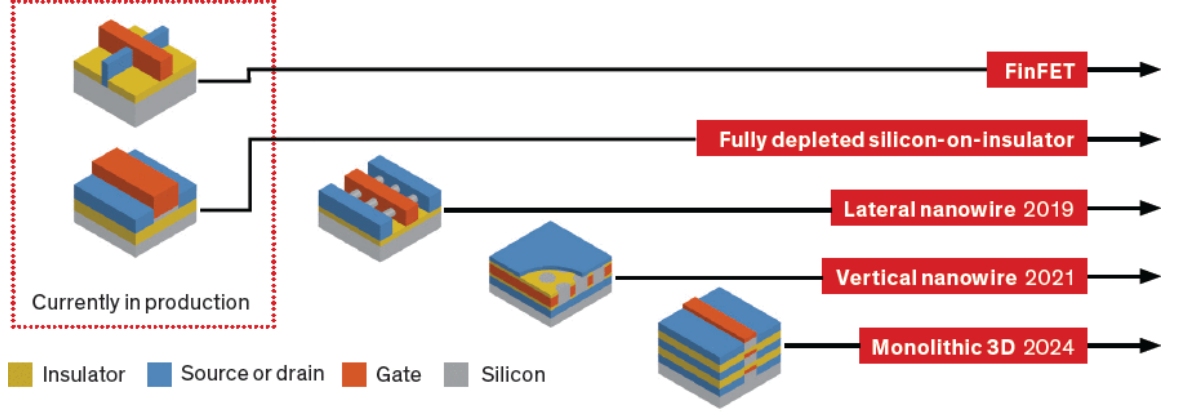


Figure 1.1: Transistor Architectures for present and future generations

Progress in the nanofabrication technology has paved a way for the use of silicon nanowire in present and future generation electronics [5]. Due to the various possibilities in device architecture and their design, physics based modelling is very important. Several groups have worked on modelling quantum transport in SNWTs using different mathematical framework like NEGF [5] [6] [7] [8] [9], Pauli master equation method or Wigner function method, etc.

The main objective of this thesis is to explore the device physics of silicon nanowire transistors through computer-based numerical simulations in the NEGF framework. The developed simulation tool is then used to study the effects of self-heating on the device characteristics.

1.2 Device, its Physics and the simulation technique

1.2.1 The Device

Figure 1.2 shows the device (courtesy[10]) for which the simulation tool is built. A SOI substrate is surrounded by insulator/gate from four sides i.e there are four gates, which are expected to increase the control of gate over the channel and reduce leakage.

The source and drain regions are doped heavily. The channel is undoped which makes it fully depleted, which is supposed to increase the mobility of charge carriers and get rid of any floating body effects [2].

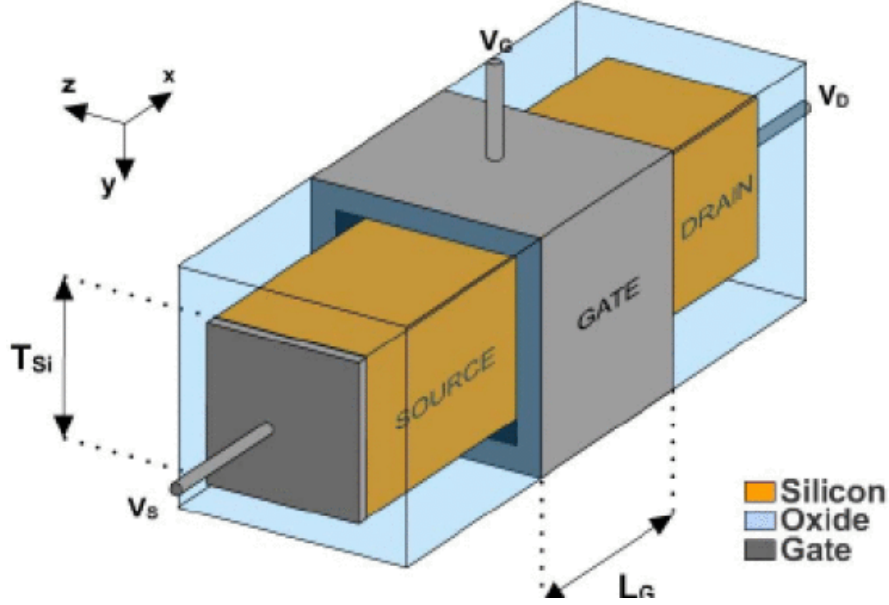


Figure 1.2: Design of Silicon Nanowire Transistor

1.2.2 Physics involved

The semi-classical theory and simulations involve solving Boltzmann Transport Equation with few or more approximations. However, in the nanoregime these approximations are no longer valid and hence it's essential to look at the problem quantum mechanically [11] [12]. Quantum approach considers the structural confinement of the charge carriers, interference faced by the wave associated with them, tunneling, etc which are not considered in the semi-classical model [13]. Therefore, it becomes necessary to solve 3D Poisson's and 3D Schrodinger's equation self-consistently for this three dimensional device .

However, solving both Poisson's and Schrodinger's in real space is both time consuming and requires huge memory. Therefore, only Poisson's equation is solved in real space while Schrodinger's equation is solved in mode-space [14] which changes the three dimensional problem to a combination of two dimensional confinement and one dimensional transport. The two dimensional confinement is considered in all cases, however, the one dimensional transport can be dealt either semi-classically or quantum mechanically.

1.2.3 Self-Consistent simulation scheme

Schrodinger's equation describes the distribution of charge but it needs the potential inside the device which is obtained from Poisson's equation which itself depends on the charge distribution. Therefore, we have a coupled problem and a self-consistent solution is required. Figure 1.3 presents the simulation procedure followed for modelling the SNWT.

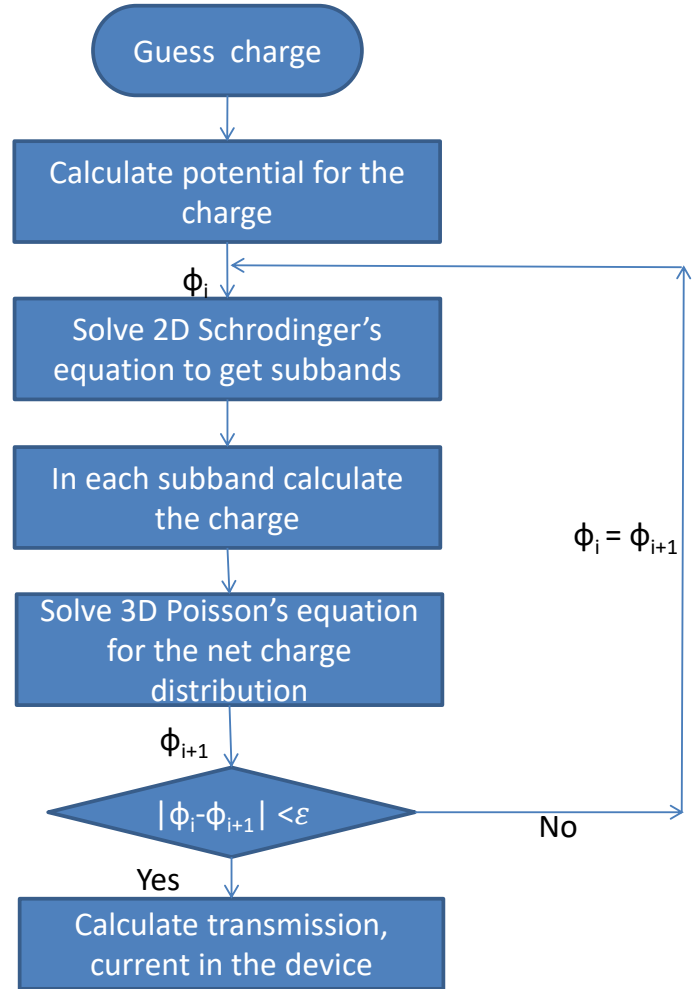


Figure 1.3: Flow chart of the self-consistent simulation scheme followed in the simulator

1.3 Overview of the thesis

1) **Chapter 2** begins with a brief introduction of the Poisson' and Schrodinger's equation in mode-space and their solution method. It is followed by a discussion on Ballistic transport in both semi-classical and quantum domain. The chapter ends with a

discussion on the validity of the semi-classical approach.

2) **Chapter 3** deals with dissipative transport. The drift-diffusion model is briefly discussed. It is followed by a discussion on modelling scattering quantum mechanically through a phenomenological method, namely, the Buttiker's probe.

3) In **Chapter 4**, using the Buttiker's probe scattering model an effort is made to understand device characteristics under thermal simulation. For this another phenomenological method, Fourier's law, is employed.

4) The thesis is concluded in **Chapter 5**. This chapter ends with a discussion on some of the possibilities for future work.

CHAPTER 2

Quantum effects and ballistic transport

For transistors operating in the nanoregime, transport may be ballistic as source to drain length becomes smaller than the mean free path. For any transistor, ballistic current sets the upper limit because charge carriers injected from both the contacts once inside the channel flow without any scattering.

The charge injected into the channel depends on the contact to channel barrier height. If the barrier is significantly higher charge carriers are scattered back into the contacts from top of the barrier. Higher gate voltage lowers the barrier height, thereby, reducing the back-scattering, resulting in more charge injection in the channel from both the contacts. But the current in the device also depends on the relative velocity of charge carriers. For high gate bias and low drain bias, comparable charge carriers are injected into the channel from both contacts resulting in lower current. For higher drain bias charge carriers are injected mostly from the source contact as the carriers from drain face a larger barrier irrespective of the gate voltage leading to a higher drain current[15][16]. However, this description is semi-classical and the current obtained from the above model for channel lengths below 10nm is lower than that observed, since there are significant quantum phenomena like tunneling and interference involved in the nano-scale which are not included in the mechanism defined above.

Irrespective of the transport mechanism, channel electrostatics is defined by the Poisson's equation. To estimate the charge in the channel three dimensional Poisson equation must be solved numerically.

2.1 Poisson's Equation

Poisson's equation relates the electrostatic potential and charge distribution and is defined as

$$\nabla(\varepsilon \nabla \Phi) = -\rho \quad (2.1)$$

where $\rho = q(p + N_d^+ - n - N_a^-)$ but the device under consideration has an undoped channel while the source and drain are doped with donor type impurities, and the hole concentration is negligible, hence, $\rho = q(N_d^+ - n)$ in the source and drain regions and $\rho = -qn$ in the channel; Φ is the unknown potential, ε is the dielectric constant of the medium which is equal to ε_{si} in silicon and ε_{ins} in the insulator. ε on the interface has to be looked at separately.

Using the finite difference method, equation 2.1 becomes

$$\begin{aligned} \frac{2\Phi_{m,n,p} - \Phi_{m-1,n,p} - \Phi_{m+1,n,p}}{(\Delta x)^2} + \frac{2\Phi_{m,n,p} - \Phi_{m,n-1,p} - \Phi_{m,n+1,p}}{(\Delta y)^2} \\ + \frac{2\Phi_{m,n,p} - \Phi_{m,n,p-1} - \Phi_{m,n,p+1}}{(\Delta z)^2} = \frac{\rho}{\varepsilon} \end{aligned} \quad (2.2)$$

The electron density term in ρ depends on the potential Φ and the Quasi-Fermi level which is defined as

$$F = -q\Phi + k_B T \mathfrak{S}_{1/2}^{-1}(n/N_c)$$

therefore

$$n = N_c \mathfrak{S}_{1/2} \left(\frac{F + q\Phi}{k_B T} \right)$$

But the Quasi-Fermi level is obtained only after the potential is known, hence this becomes a coupled problem in itself. Therefore, an iterative scheme is employed here. For the potential of the previous iteration a Quasi-Fermi is defined leading to electron density equation as

$$n = N_c \mathfrak{S}_{1/2} \left(\frac{-q\Phi_{old} + k_B T \mathfrak{S}_{1/2}^{-1}(n_{old}/N_c) + q\Phi_{new}}{k_B T} \right) \quad (2.3)$$

This results in a non-linear equation in just one variable Φ . In order to solve this non-linear equation Newton-Raphson's method is used. But before that the boundary conditions must be incorporated in the equation.

2.1.1 Boundary Conditions

Metallic Gate boundary: The potential is set equal to the gate voltage. $\Phi = V_g$

Oxide-vacuum interface: In order to make sure that electrons don't leak outside the device at the non-contacts Neumann's boundary condition is imposed i.e

$$n \cdot \nabla \Phi = 0$$

Semiconductor/oxide metallic source/drain interface: The source and drain are heavily doped but are not metal. Electrons in case of ballistic transport are under non-equilibrium and are supplied by diffusion current so in order to ensure that no drift current flows from contacts into the device Neumann's boundary condition is imposed at these contacts i.e.

$$n \cdot \nabla \Phi = 0$$

Semiconductor oxide interface: The value of dielectric constant ε is not defined at the interface. This is dealt by considering a finite element method based on flux balance on a finite volume which reduces to Gauss' law for steady-state conditions[12].

$$Q_{enclosed} = \varepsilon \oint E \cdot dS$$

Now assuming an imaginary cuboid of volume $\Delta x \Delta y \Delta z$ centered at every grid point on the interface. The cuboid is divided into eight mini-cuboids each representing a different material and hence a different ε . Finally using the flux balance method get

$$\begin{aligned} (\Delta x \Delta y \Delta z) n_{n,m,p} = & \frac{1}{4} \left[-\Phi_{m,n,p} \left(\frac{\Delta y \Delta z}{\Delta x} + \frac{\Delta x \Delta z}{\Delta y} + \frac{\Delta x \Delta y}{\Delta z} \right) \left(\sum_{i=1}^8 \varepsilon_i \right) + \right. \\ & \Phi_{m+1,n,p} (\varepsilon_1 + \varepsilon_4 + \varepsilon_5 + \varepsilon_8) \frac{\Delta y \Delta z}{\Delta x} + \Phi_{m-1,n,p} (\varepsilon_2 + \varepsilon_3 + \varepsilon_5 + \varepsilon_7) \frac{\Delta y \Delta z}{\Delta x} + \\ & \Phi_{m,n+1,p} (\varepsilon_1 + \varepsilon_2 + \varepsilon_5 + \varepsilon_6) \frac{\Delta x \Delta z}{\Delta y} + \Phi_{m,n-1,p} (\varepsilon_3 + \varepsilon_4 + \varepsilon_7 + \varepsilon_8) \frac{\Delta x \Delta z}{\Delta y} + \\ & \left. \Phi_{m,n,p+1} (\varepsilon_1 + \varepsilon_2 + \varepsilon_3 + \varepsilon_4) \frac{\Delta x \Delta y}{\Delta z} + \Phi_{m,n,p-1} (\varepsilon_5 + \varepsilon_6 + \varepsilon_7 + \varepsilon_8) \frac{\Delta x \Delta y}{\Delta z} \right] \end{aligned}$$

This equation reduces to equation 2.2 ε_i is set to the appropriate value i.e. ε_{Si} or ε_{ins}

2.1.2 Solving the equation

Once the boundary conditions are incorporated in the Poisson's equation, the next step is to solve this non-linear equation using the Newton-Raphson's method. The equation is given as:

$$\begin{aligned}
 f_{\alpha} = & \frac{1}{4} \left[-\Phi_{m,n,p} \left(\frac{\Delta y \Delta z}{\Delta x} + \frac{\Delta x \Delta z}{\Delta y} + \frac{\Delta x \Delta y}{\Delta z} \right) \left(\sum_{i=1}^8 \varepsilon_i \right) + \right. \\
 & \Phi_{m+1,n,p} (\varepsilon_1 + \varepsilon_4 + \varepsilon_5 + \varepsilon_8) \frac{\Delta y \Delta z}{\Delta x} + \Phi_{m-1,n,p} (\varepsilon_2 + \varepsilon_3 + \varepsilon_6 + \varepsilon_7) \frac{\Delta y \Delta z}{\Delta x} + \\
 & \Phi_{m,n+1,p} (\varepsilon_1 + \varepsilon_2 + \varepsilon_5 + \varepsilon_6) \frac{\Delta x \Delta z}{\Delta y} + \Phi_{m,n-1,p} (\varepsilon_3 + \varepsilon_4 + \varepsilon_7 + \varepsilon_8) \frac{\Delta x \Delta z}{\Delta y} + \\
 & \left. \Phi_{m,n,p+1} (\varepsilon_1 + \varepsilon_2 + \varepsilon_3 + \varepsilon_4) \frac{\Delta x \Delta y}{\Delta z} + \Phi_{m,n,p-1} (\varepsilon_5 + \varepsilon_6 + \varepsilon_7 + \varepsilon_8) \frac{\Delta x \Delta y}{\Delta z} \right] \\
 & - (\Delta x \Delta y \Delta z) n_{n,m,p}
 \end{aligned} \tag{2.4}$$

Solving f_{α} means putting $f_{\alpha} = 0$ to get a value of potential. This, however, is not straight forward and is carried out iteratively by linearizing the equation about some x_0 according to

$$f(x_0 + h) \approx f(x_0) + f'(x_0) * h$$

Now putting $f(x_0 + h) = 0$ results in $h = -f(x_0)/f'(x_0)$. Therefore,

$$f_{\alpha}(\Phi_{new}) \approx f_{\alpha}(\Phi_{old}) + f_{\alpha,\beta}(\Phi_{old}) * (\Phi_{new} - \Phi_{old})$$

where

$$f_{\alpha,\beta} = \partial f_{\alpha} / \partial \Phi_{\beta}$$

is the Jacobian matrix consisting of all the first order derivative of f_{α} with respect to every other grid voltage Φ_{β} . Therefore,

$$\Delta \Phi = -f_{\alpha}(\Phi_{old}) / f_{\alpha,\beta}(\Phi_{old}) \tag{2.5}$$

2.2 Schrodinger's Equation

Schrodinger's equation must be solved in order to incorporate any quantum effect. It dictates the charge distribution in the device. The time-dependent Schrodinger's wave equation is

$$i\hbar \frac{\partial \Psi}{\partial t} = -\frac{\hbar^2}{2} \nabla \left(\frac{1}{m} \nabla \Psi \right) + U\Psi \quad (2.6)$$

where U is the potential energy term.

But as stationary solutions are desired here, equation 2.6 reduces to

$$-\frac{\hbar^2}{2} \nabla \left(\frac{1}{m} \nabla \Psi \right) + U\Psi = E\Psi \quad (2.7)$$

It is, however, unrealistic to find an explicit solution for the stationary Schrodinger's equation. The solutions are instead expressed in terms of known basis functions. Every simulator that solves a Schrodinger's equation uses some basis function, hence it's the choice of the basis function that makes each simulator unique.

Since the system is composed of atoms the first choice would be the atomic orbital wave functions but the coupling between the orbitals must be obtained from first principle or empirically. Therefore, in this simulator a simple and memory efficient model, viz. an effective mass model is employed, which basically takes into account the perturbation of the atomic potential in the rest mass of the electrons leading to an effective mass value. The equation therefore becomes

$$-\frac{\hbar^2}{2} \nabla \left(\frac{1}{m^*} \nabla \Psi \right) + U\Psi = E\Psi \quad (2.8)$$

m^* takes different values in silicon and insulator regions. On the interface however, it is the average of the mass of electrons in silicon and insulator.

For the three dimensional device as in figure 1.2, the equation that must be solved is

$$H_{3D}\Psi(x, y, z) = E\Psi(x, y, z) \quad (2.9)$$

$$\text{where } H_{3D} = -\frac{\hbar^2}{2m_x^*} \frac{\partial^2}{\partial x^2} - \frac{\hbar^2}{2} \frac{\partial}{\partial y} \left(\frac{1}{m_y^*} \frac{\partial}{\partial y} \right) - \frac{\hbar^2}{2} \frac{\partial}{\partial z} \left(\frac{1}{m_z^*} \frac{\partial}{\partial z} \right) + U(x, y, z)$$

here $U(x,y,z)$ is the potential energy term obtained from the Poisson's equation. It is basically the conduction band-edge profile. m_x^* , m_y^* , m_z^* are the effective mass of electron in the x,y and z direction respectively. Along the y and z directions the effective mass is not the same but changes from silicon region to the insulator region.

Now, the solution to equation 2.9 should give the desired result but the size of the Hamiltonian becomes $(N_x \times N_y \times N_z)^2$ on a real-space grid of size $(N_x \times N_y \times N_z)$. Solving this is time consuming and highly memory inefficient. It is, therefore, desirable to find a scheme that reduces computational burden.

2.2.1 Mode Space Approach

In thin devices like the one under consideration, due to the confinement effects along the y,z directions electrons flow in discrete energy levels called subbands. Taking advantage of this situation, the device Hamiltonian is expanded in subband eigenfunction space[5][12][13][14].

In real space the Hamiltonian can be expanded in terms of $\delta(x-x')\delta(y-y')\delta(z-z')$ where x',y',z' are the eigenvalues of the Hamiltonian. The modes(subbands) replace $\delta(y-y')\delta(z-z')$, and the 3D wave function

$$\Psi(x', y, z) = \sum_n \varphi^n(x') \xi^n(y, z, x') \quad (2.10)$$

expanded in the subband eigen space at any $x = x'$ leads to final 2D Schrodinger's equation of the form

$$\left[-\frac{\hbar^2}{2} \frac{\partial}{\partial y} \left(\frac{1}{m_y^*} \frac{\partial}{\partial y} \right) - \frac{\hbar^2}{2} \frac{\partial}{\partial z} \left(\frac{1}{m_z^*} \frac{\partial}{\partial z} \right) + U(x', y, z) \right] \xi^n(y, z, x') = E_{sub}^n \xi^n(y, z, x') \quad (2.11)$$

where $\xi^n(y, z, x')$ is the n^{th} eigen function and E_{sub}^n is the n^{th} subband energy level at slice $x = x'$ of the SNWT.

Using equations (2.10), (2.11) in (2.9) results in

$$-\frac{\hbar^2}{2m_x^*} \frac{\partial^2}{\partial x^2} \left(\sum_n \varphi^n(x) \xi^n(y, z, x) \right) + \sum_n \varphi^n(x) E_{sub}^n \xi^n(y, z, x) = E \sum_n \varphi^n(x) \xi^n(y, z, x) \quad (2.12)$$

Now multiplying by $\xi^m(y, z, x)$ and integrating in the y-z plane leads to a 1D coupled Schrodinger's equation with open boundaries

$$\begin{aligned} & \frac{-\hbar^2}{2} \left(\sum_{n=1}^{\infty} a_{mn}(x) \right) \frac{\partial^2}{\partial x^2} \varphi^m(x) - \frac{\hbar^2}{2} \sum_n c_{mn}(x) \varphi^n(x) \\ & - \hbar^2 \sum_n b_{mn}(x) \frac{\partial}{\partial x} \varphi^n(x) + E_{sub}^m \varphi^m(x) = E \varphi^m(x) \end{aligned} \quad (2.13)$$

where $a_{mn}(x)$, $b_{mn}(x)$, $c_{mn}(x)$ are as defined in [5].

Now, equation (2.13) represents **Coupled Mode Space(CMS)** and yields the same result as the real-space solution if all the modes are considered i.e $m, n = 1, 2, 3, \dots N_{YZ}$. However, for thin devices due to strong confinement only few lowest modes are occupied i.e $m, n = 1, 2, 3 \dots M$ where $M \ll N_{YZ}$ and the higher modes are almost vacant. This reduces the computation cost as the size of the 1D coupled Hamiltonian now becomes $(M \times N_x)^2$ instead of $(N_x \times N_y \times N_z)^2$. It is shown in [13] [14], that the real space solution and CMS solution match perfectly.

Assuming the device is uniform along the transport direction x, it is shown in [5] and [13] that the conduction band profile varies very slowly along x and has the same shape at all x. This assumption leads to approximately the same eigen function $\xi^m(y, z; x)$ at all x along the channel but with different eigenvalues $E_{sub}^m(x)$. This results in

$$\frac{\partial}{\partial x} \xi^m(y, z, x) = 0 \quad (2.14)$$

Hence equation 2.13 simplifies to

$$\frac{-\hbar^2}{2} \left(\sum_{n=1}^{\infty} a_{mn}(x) \right) \frac{\partial^2}{\partial x^2} \varphi^m(x) + E_{sub}^m \varphi^m(x) = E \varphi^m(x) \quad (2.15)$$

This has simplified the problem even further by uncoupling the subbands at different x, hence this is known as **Uncoupled Mode Space(UMS)**. It is shown in [5] and [13]

that CMS and UMS results match well for thin body devices, where due to confinement bands are far apart and hence there is no inter subband interaction.

The simulation tool developed as part of this thesis employs UMS and therefore is valid only for thickness less than 5nm because for greater thickness the confinement effects are lower and bands are comparatively closer which violates the assumption of no inter-subband interaction.

2.2.2 Implementation

Figure 2.1 shows the grid structure at every x where the 2D Schrodinger's equation 2.11 is solved for eigen values and eigen functions. U in the equation is the potential obtained from Poisson's equation. The blue region represents silicon while the red represents insulator. In the simulator, it's possible to include electron penetration in the oxide or neglect it. Considering electron penetration shows the finite nature of the barrier while neglecting electron penetration assumes that the barrier between oxide and the semiconductor is infinite. There is no leakage current, however, in either case.

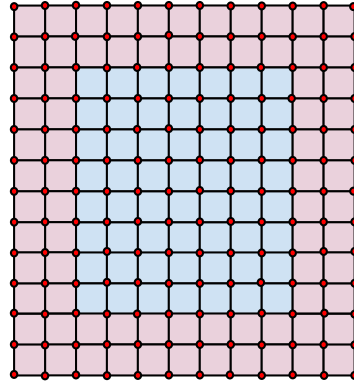


Figure 2.1: Grid structure at every x . 2D Schrodinger's equation is solved on this grid using FDM

2.3 Transport

The modelling problem which was three dimensional reduces to one-dimensional transport after solving the 2D Schrodinger's equation at every x in the device. Transport can now be modelled either as ballistic or diffusive. This chapter focuses on ballistic

transport - both semi-classical and quantum mechanical.

2.3.1 Semi-classical Ballistic Transport

Semi-classical theory treats electrons as particles. In ballistic transport electrons travel through the channel without losing any momentum or energy. Electrons, which are in thermal equilibrium are injected into the channel by the contacts. However, in case of ballistic transport electrons in the channel are out of equilibrium as there is no scattering in the channel to keep them in thermal equilibrium with the contacts.

To treat such a transport mathematically, Boltzmann's transport equation is solved in the ballistic limit. As shown in figure 2.2, injected carriers from both source and drain either transmit through to the other contact if they are above the barrier or get reflected back from the barrier into the contacts, which are perfect absorbers. Now, the electron distribution in the source(drain) contact are described by source(drain) Fermi function. But to describe electrons in the channel, there isn't one function instead all electrons above the barriers moving from source(drain) to drain(source) are defined by source(drain) Fermi function. While electrons injected from the source(drain) which are below the barrier and get reflected are defined by only the source(drain) Fermi function[11].

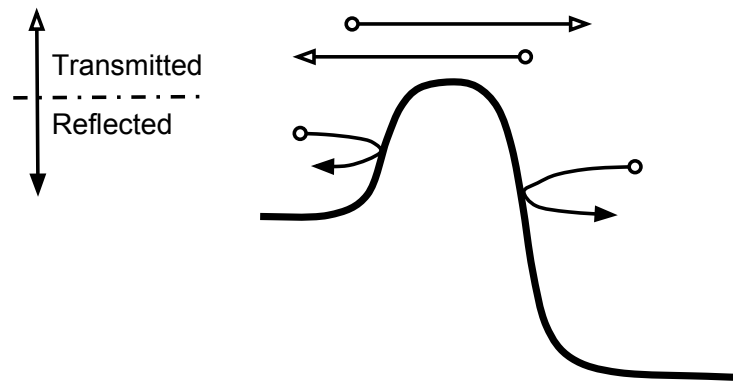


Figure 2.2: Charge transport in the top of the barrier model

In the simulation tool, charge and current in the top of the barrier model are calculated in each subband obtained after solving the 2D Schrodinger's equation on the grid as in figure 2.1 and then summed over to get the final charge distribution in the

subbands.

Calculating the charge

The electron density $n(E)$ at any energy level E , depends on the density of states $D(E)$ and the distribution function $f(E)$ and is defined as their product

$$n(E) = D(E)f(E) \quad (2.16)$$

Any point A(B) on the left(right) of the source(drain)- channel barrier has three kinds of electron - right(left) moving electrons due to the source(drain), left(right) moving electrons due to the drain(source) above the barrier, and both left and right moving electrons due to the source(drain) below the barrier.

So for any subband i , 1D electron density at A is given by

$$n_i(A) = \int_0^\infty D_{1D}(E)f_s(E)dE + \int_0^{E_{top}} D_{1D}(E)f_s(E)dE + \int_{E_{top}}^\infty D_{1D}(E)f_d(E)dE \quad (2.17)$$

$$\text{where } D_{1D}(E) = \frac{1}{\pi\hbar} \sqrt{\frac{m_x^*}{2E}}, \quad f_s(E) = \frac{1}{1+e^{\frac{E+E_i-\mu_s}{kT}}} \quad \text{and} \quad f_d(E) = \frac{1}{1+e^{\frac{E+E_i-\mu_d}{kT}}}$$

Therefore,

$$\begin{aligned} n_i(A) = & \int_0^\infty \frac{1}{\pi\hbar} \sqrt{\frac{m_x^*}{2E}} \frac{1}{1+e^{\frac{E+E_i-\mu_s}{kT}}} dE \\ & + \int_0^{E_{top}} \frac{1}{\pi\hbar} \sqrt{\frac{m_x^*}{2E}} \frac{1}{1+e^{\frac{E+E_i-\mu_s}{kT}}} dE \\ & + \int_{E_{top}}^\infty \frac{1}{\pi\hbar} \sqrt{\frac{m_x^*}{2E}} \frac{1}{1+e^{\frac{E+E_i-\mu_d}{kT}}} dE \end{aligned} \quad (2.18)$$

The infinity in the integral as in equation 2.18 is replaced by a large value of E where f_s, f_d go to zero. To evaluate the above integral numerically, an approximate expression is used as given below

$$\int_a^b g(x)dx \approx \left[g\left(a + \sum_{k=0}^n k\left(\frac{b-a}{n}\right)\right) - \frac{g(a) + g(b)}{2} \right] \left(\frac{b-a}{n}\right)$$

The above evaluation gives the charge in a subband. Now the charge in individual subbands in every valleys must be added to get the final one dimensional charge distri-

bution, which is finally distributed in the entire device using the eigen wave functions obtained from the 2D Schrodinger's equation. A factor of 2 to consider spin degeneracy must be included as well separately.

$$n_{3D}(x', y, z) = 2 \sum_i n_i(x') \frac{|\xi(y, z, x')|^2}{dy * dz} \quad (2.19)$$

where x' may represent A or B.

Once the 3D charge density in the device is obtained, the quasi-fermi level corresponding to it can be calculated which can then be used by Poisson's equation to get the potential profile in the device.

Calculating the current

Once the final value of potential is obtained for a given convergence criterion, current is calculated individually in every subband in every valley and finally added up to get the final result. A factor of 2 for spin degeneracy is included here as well.

Current is the rate of flow of charge. Only the electrons above the barrier contribute to the current. Hence, current depends on the net electrons crossing any point and the speed with which they flow. Group velocity of an electron at the bottom of the conduction band can be calculated as $v = \frac{1}{\hbar} \frac{dE}{dk}$. For parabolic band approximation $E = \frac{\hbar^2 k^2}{2m^*}$. Hence,

$$v = \frac{\hbar k}{m^*} = \sqrt{\frac{2E}{m^*}} \quad (2.20)$$

Since there is no scattering inside the device for ballistic case, current is same everywhere inside the channel[12], hence current is calculated in a subband i at some $x = x'$ as

$$I_i = qvn_i(x') = \int_{E_{top}}^{\infty} q \sqrt{\frac{2E}{m_x^*}} \frac{1}{\pi \hbar} \sqrt{\frac{m_x^*}{2E}} (f_s(E) - f_d(E)) dE \quad (2.21)$$

$$I_i = q \frac{1}{\pi \hbar} \int_{E_{top}}^{\infty} \left[\frac{1}{1 + \exp\left(\frac{E_i + E - \mu_s}{kT}\right)} - \frac{1}{1 + \exp\left(\frac{E_i + E - \mu_d}{kT}\right)} \right] dE \quad (2.22)$$

The above equation simplifies to

$$I_i = \frac{q}{\pi \hbar} k_B T \left[\ln \left[1 + \exp\left(-\frac{E_{top} + \mu_s}{kT}\right) \right] - \ln \left[1 + \exp\left(-\frac{E_{top} + \mu_d}{kT}\right) \right] \right] \quad (2.23)$$

The net current is therefore given as

$$I = 2 \sum_{i=1}^M I_i \quad (2.24)$$

Note: In the codes, valley degeneracy is assumed when calculating charge and current, hence, a factor of 2 comes for valley degeneracy as well along with the factor for spin degeneracy.

For the semi-classical model described, figure 2.3 shows the current vs. voltage curve for a 10 nm channel length, $3nm \times 3nm$ silicon cross-section; figure 2.4 shows the first subband variation along the transport direction with drain voltage and figure 2.5 shows the variation of 1D electron charge density along x with drain voltage for the above mentioned device features.

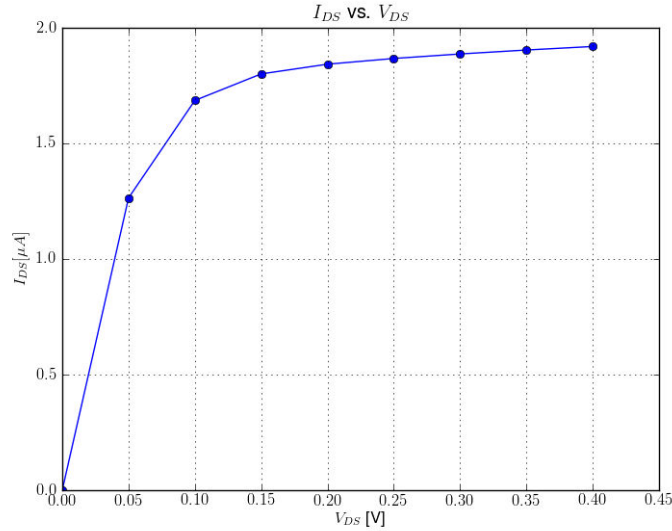


Figure 2.3: I_D vs. V_D for a 10 nm channel length

2.3.2 Quantum Ballistic Transport

In the nanoregime, canonical equation like the BTE are no longer valid because the wave nature of electrons become significant. There are several quantum phenomena like tunneling, interference, discrete energy levels due to confinement that can't be explained by the semi-classical theory.

In the developed simulator, there is no pure semi-classical approach because along with a 3D Poisson's equation that governs the electrostatics of the device, a 2D Schrodinger's

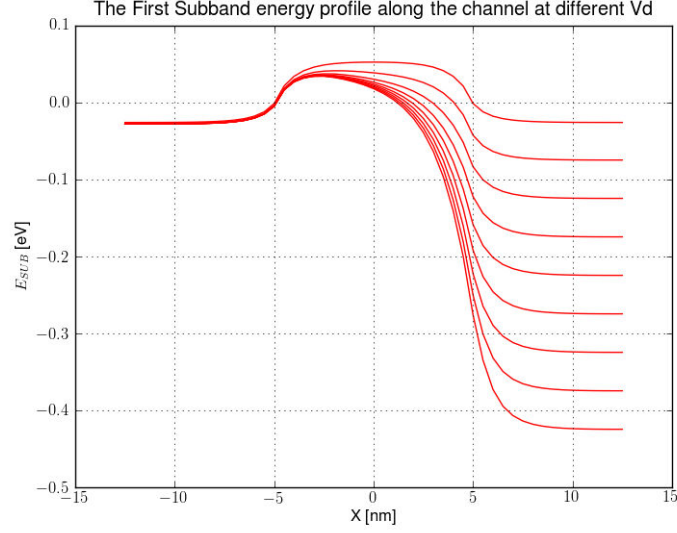


Figure 2.4: First subband variation vs. V_D for a 10nm channel length

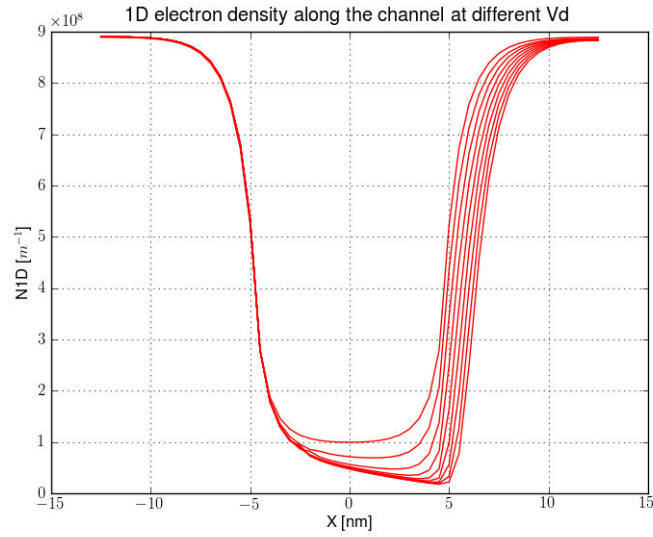


Figure 2.5: Electron charge concentration variation vs. V_D for a 10nm channel length

equation is solved along the transport direction at every x . It's only the transport that is treated semi-classically or quantum mechanically. In the semi-classical approach as discussed in the previous section, BTE is used to describe 1D transport while quantum mechanically 1D Schrodinger equation describes the transport.

Contrary to the semi-classical theory now consider electron waves incident from source and drain contacts into the channel. Some portion of both the incident waves gets reflected back to the parent contact while the remaining gets transmitted to the other contact [11]. Let the wave function in device due to source and drain be Ψ_D^s and Ψ_D^d respectively. In addition to them, because of electron-phonon, electron-electron

interaction (scattering), localized and quasi-localized states are filled and these states are represented by Ψ_D^{loc} . In ballistic and quasi-ballistic transport, Ψ_D^{loc} is absent i.e there is no scattering. Due to the mentioned wave functions the electron density and current density along the transport direction are given as

$$n(x) = \sum_{k,s} [|\Psi_D^s(x)|^2 f_s(E) + |\Psi_D^d(x)|^2 f_d(E)] \quad (2.25)$$

and

$$J(x) = \sum_{k,s} \left[\Psi_D^s(x)^\dagger \frac{d\Psi_D^s(x)}{dx} f_s(E) + \Psi_D^d(x)^\dagger \frac{d\Psi_D^d(x)}{dx} f_d(E) - c.c \right] \quad (2.26)$$

where k, s represent sum on the momentum and spin states; $f_s(E)$ and $f_d(E)$ are Fermi distribution of the source and the drain contacts; $c.c$ represents the complex conjugate of the first two terms. Since there are no spin dependent phenomena considered the sum on ‘ s ’ simplifies as a factor of 2.

Now, obtaining an explicit expression of wave functions in the device is difficult hence Non Equilibrium Green’s Function (NEGF) technique is employed to address the problem[17]. 3D Schrodinger equation is solved as 2D Schrodinger’s equation in a cross-section and 1D transport in the subbands obtained from 2D equation. This 1D transport is solved using the NEGF framework.

Start with equation(2.13)

$$\begin{aligned} & -\frac{\hbar^2}{2} \left(\sum_{n=1}^{\infty} a_{mn}(x) \right) \frac{\partial^2}{\partial x^2} \varphi^m(x) - \frac{\hbar^2}{2} \sum_n c_{mn}(x) \varphi^n(x) \\ & - \hbar^2 \sum_n b_{mn}(x) \frac{\partial}{\partial x} \varphi^n(x) + E_{sub}^m \varphi^m(x) = E \varphi^m(x) \end{aligned} \quad (2.27)$$

where

$$a_{mn}(x) = \oint_{y,z} \frac{1}{m_x^*(y,z)} \xi^m(y,z,x) \xi^n(y,z,x) dy dz \quad (2.28)$$

$$b_{mn}(x) = \oint_{y,z} \frac{1}{m_x^*(y,z)} \frac{\partial \xi^m(y,z,x)}{\partial x} \frac{\partial \xi^n(y,z,x)}{\partial x} dy dz \quad (2.29)$$

$$c_{mn}(x) = \oint_{y,z} \frac{1}{m_x^*(y,z)} \frac{\partial^2 \xi^m(y,z,x)}{\partial x^2} \xi^n(y,z,x) dydz \quad (2.30)$$

Equation 2.27 corresponds to coupled mode space (CMS) and is equivalent to real-space solution if all the modes ($m = 1, 2, 3 \dots N_{YZ}$) are taken into account. However, in case of thin devices because of strong confinement only few lower modes ($m = 1, 2, 3, \dots M$ where $M \ll N_{YZ}$) are occupied. In addition to this, since most of the wave function is located in the silicon region for $m \neq n$, a_{mn} can be neglected ($a_{mm} \gg a_{mn}$)[5].

Equation 2.27 represents a group of M equations for each of the M subbands and can be written as $H\Phi = E\Phi$, where any element h_{mn} of H can be represented as

$$h_{mn} = -\frac{\hbar^2}{2} a_{mn} \frac{\partial^2}{\partial x^2} + E_{sub}^m(x) - \frac{\hbar^2}{2} c_{mn}(x) - \hbar^2 b_{mn}(x) \frac{\partial}{\partial x} \quad (2.31)$$

However, for a thin, uniform device like the one presented in this work, further approximation (equation 2.14) results in Uncoupled mode space (UMS) (equation 2.15)

$$\frac{-\hbar^2}{2} \left(\sum_{n=1}^{\infty} a_{mn}(x) \right) \frac{\partial^2}{\partial x^2} \varphi^m(x) + E_{sub}^m \varphi^m(x) = E \varphi^m(x)$$

Again if $m \neq n$, a_{mn} can be neglected ($a_{mm} \gg a_{mn}$). This therefore, gives

$$h_{mn} = -\frac{\hbar^2}{2} a_{mn} \frac{\partial^2}{\partial x^2} + E_{sub}^m(x) \quad (2.32)$$

where

$$a_{mm}(x) = \oint_{y,z} \frac{1}{m_x^*(y,z)} |\xi^m(y,z,x)|^2 dydz \quad (2.33)$$

Therefore, $h_{mn} = 0$ if $m \neq n$ and H becomes a diagonal matrix. Now this equation is discretized as per finite difference method but there is an issue at the contact boundary as there is no knowledge of the connection between the device and the contacts.

The NEGF method as described in [5] [13][17][18] uses the ‘Self Energy’ concept to terminate the otherwise infinite H matrix. The self energy term connects the device to the semi-infinite contacts and describes its interaction with the outside world. It is also used to describe the ‘localized’ processes (scattering) going on in the device. In

ballistic case however, these localized processes are absent.

Finally, the Green's function is defined as

$$G[EI - H - \Sigma_s(E) - \Sigma_c(E)] = I \quad (2.34)$$

where G is the retarded Greens' function, H is the device Hamiltonian as described by equation 2.32, Σ_s is the scattering self-energy (zero in ballistic case), and Σ_c is the contact self energy. So $G = [EI - H - \Sigma_s(E) - \Sigma_c(E)]^{-1}$

Now using FDM, self-energy for source contact is defined as

$$\Sigma_1[p, q] = -t_{m,1} \exp(jk_{m,1}a) \delta_{p,(m-1)N_x+1} \delta_{q,(m-1)N_x+1} \quad (2.35)$$

and for drain contact it is defined as

$$\Sigma_2[p, q] = -t_{m,N_x} \exp(jk_{m,N_x}a) \delta_{p,(m-1)N_x} \delta_{q,(m-1)N_x} \quad (2.36)$$

where $m = 1, 2, 3, \dots, M$ and $p, q = 1, 2, 3, \dots, MN_x$

$t_{m,1} = \frac{\hbar^2}{2a^2} a_{mm}|_{x=0}$; $t_{m,N_x} = \frac{\hbar^2}{2a^2} a_{mm}|_{x=N_x-1}$; $k_{m,1}, k_{m,N_x-1}$ are defined by $E = E_{sub}^m(0) + 2t_{m,1}(1 - \cos(k_{m,1}a))$ at source end and $E = E_{sub}^m((N_x - 1)a) + 2t_{m,1}(1 - \cos(k_{m,N_x}a))$ at drain end.

After evaluating the above quantities, the spectral density function due to source and drain contact is then defined as

$$A_1^m(E) = G(E)\Gamma_1^m(E)G^\dagger(E) \quad \text{and} \quad A_2^m(E) = G(E)\Gamma_2^m(E)G^\dagger(E) \quad (2.37)$$

where $\Gamma_i^m(E) = j(\Sigma_i^m(E) - \Sigma_i^{m\dagger}(E)) = -2\text{Im}(\Sigma_i^m(E))$, $i = 1, 2$. Γ_i represents the electron exchange rate between the device and source/drain contacts. Now, define the Local Density of states for mode m for the source D_1^m , for the drain D_2^m as

$$D_1^m[p] = \frac{1}{2\pi a} A_1^m[p, p] \quad (2.38)$$

$$D_2^m[p] = \frac{1}{2\pi a} A_2^m[p, p] \quad (2.39)$$

Hence, the diagonal element of the spectral density function represents the LDOS. Now, in order to find the electron density, define 1D electron density in mode m as

$$n_{1D}^m = 2 \int_0^\infty [D_1^m(E)f(\mu_1, E) + D_2^m(E)f(\mu_2, E)] dE \quad (2.40)$$

where $f(\mu_1, E)$ and $f(\mu_2, E)$ are the Fermi functions at source and drain respectively and a factor of 2 is included for spin degeneracy.

The 3D electron density in mode m can then be obtained as

$$n_{3D}^m = n_{1D}^m |\xi(y, z, x)|^2 / (dy \times dz) \quad (2.41)$$

In order to get the electron density in the device, sum over all the subbands and valleys (degeneracy factor of 2) to get the final three dimensional charge distribution. This 3D charge distribution is then fed to the Poisson's equation to get the final potential in the device. After a consistency is achieved in potential and charge, current in each subband is calculated as

$$I^m = \frac{2q}{2\pi\hbar} \int_{-\infty}^\infty T^m(E) [f_1(\mu_1, E) - f_2(\mu_2, E)] dE \quad (2.42)$$

where $T_m(E)$ is the transmission probability in mode m and is calculated as

$$T^m(E) = \text{Trace} [\Gamma_1^m(E) G^m(E) \Gamma_2^m(E) G^{m\dagger}(E)] \quad (2.43)$$

To get the final current, contribution from all valleys (factor of 2 for valley degeneracy) and subbands must be taken into account

$$\mathbf{I} = 2 \sum_{m=1}^{m=M} I^m \quad (2.44)$$

For the quantum ballistic model discussed, figure 2.6 shows the current vs. gate voltage curve for a $10nm$ channel and $3nm \times 3nm$ silicon cross-section, figure 2.8 shows the variation of charge in the first subband with gate voltage and figure 2.7 shows the first subband variation along the transport direction with gate voltage

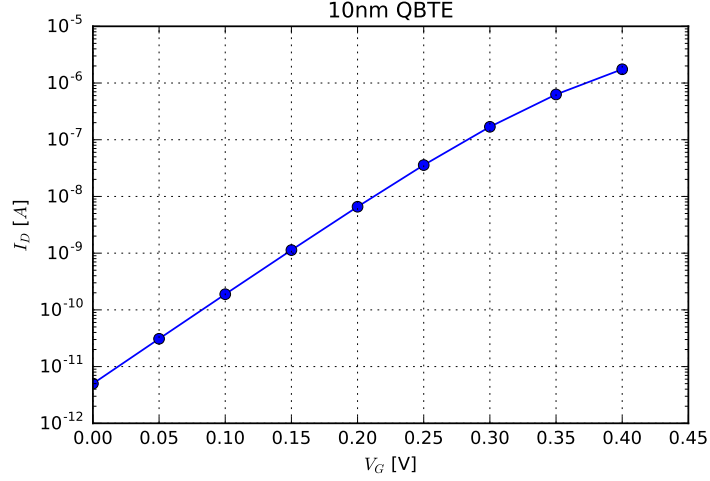


Figure 2.6: qbte:Current vs. Gate voltage for a 10nm device for quantum ballistic model

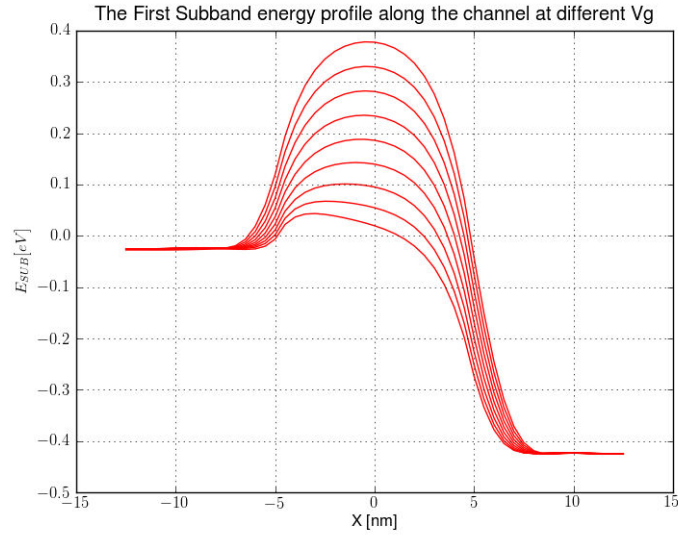


Figure 2.7: qbte:First subband variation vs. V_G for a 10nm channel length

2.4 Bench marking, Comparisons and Validation

Now that both the semi-classical and the quantum mechanical approaches are discussed, it is necessary to compare them and state their validity, however, before doing so the quantum ballistic model is compared to the simulator available on nanohub.org [19] for bench marking purpose.

2.4.1 Bench marking

Figures 2.9, 2.10, 2.11, and 2.12 show the comparison between the results obtained from the developed simulator and the simulator from nanohub. It can be easily

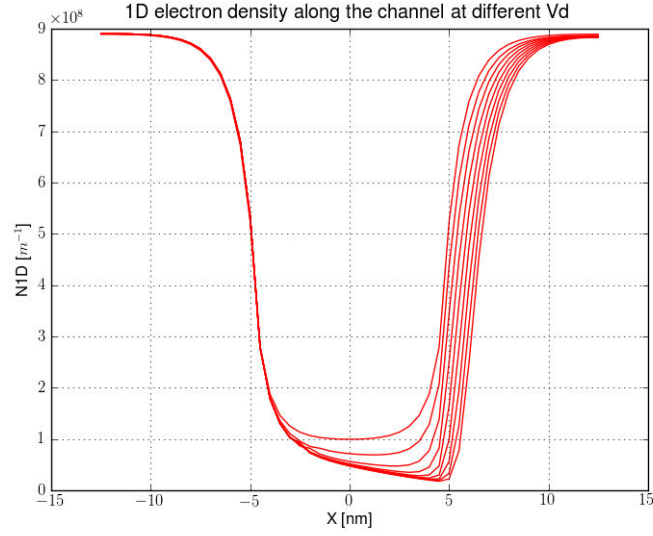


Figure 2.8: qbte:Electron charge concentration variation vs. V_G for a 10nm channel length

verified that the results are in close agreement and the variation might be because of the difference in the values of conduction band offset, grid spacing, differences in boundary conditions as these quantities were not clearly mentioned in the cited source.

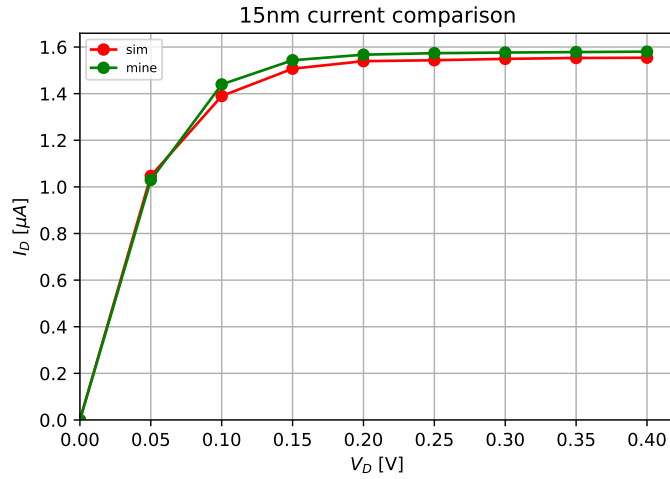


Figure 2.9: Current voltage curve for a 3nm x 3nm Silicon body cross-section and 15 nm channel length

2.4.2 Semi-classical and Quantum ballistic transport

Now that the quantum ballistic model has been benchmarked against a credible source, the next step is to compare the results of the semi-classical and quantum ballistic transport.

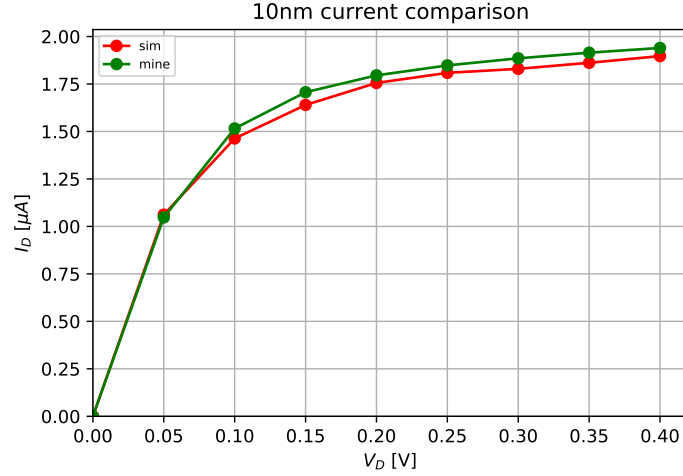


Figure 2.10: Current voltage curve for a 3nm x 3nm Silicon body cross-section and 10 nm channel length

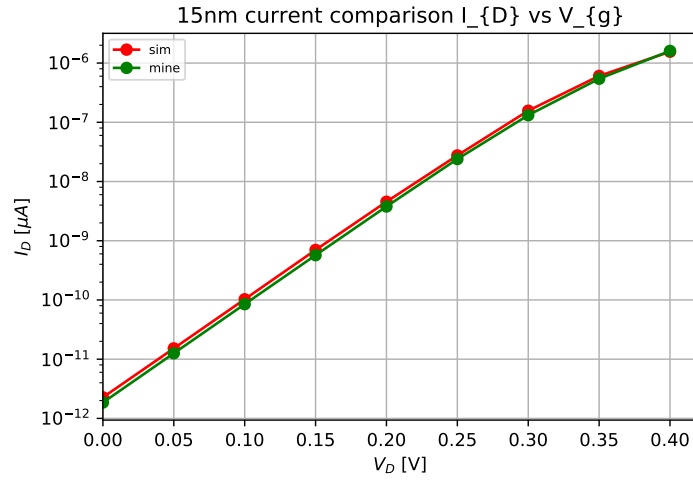


Figure 2.11: Current voltage curve for a 3nm x 3nm Silicon body cross-section and 15 nm channel length

Figures 2.13, 2.14 and 2.15 show the current-drain voltage for the quantum ballistic and the semi-classical ballistic case for different channel length. For 15nm and 10 nm the results of both the semi-classical and quantum models are close to each other but 5nm channel length shows a big variation in the results of the two models raising questions about the validity of the semi-classical approach.

Figure 2.16 shows that the result of the semi-classical and quantum model are in good agreement while figure 2.17 shows slight variation indicating presence of quantum mechanical phenomena which the semi-classical model fails to capture. Finally, figure 2.18 shows clearly the presence of tunneling current. All the results stated here are for a Silicon cross-section of $3nm \times 3nm$

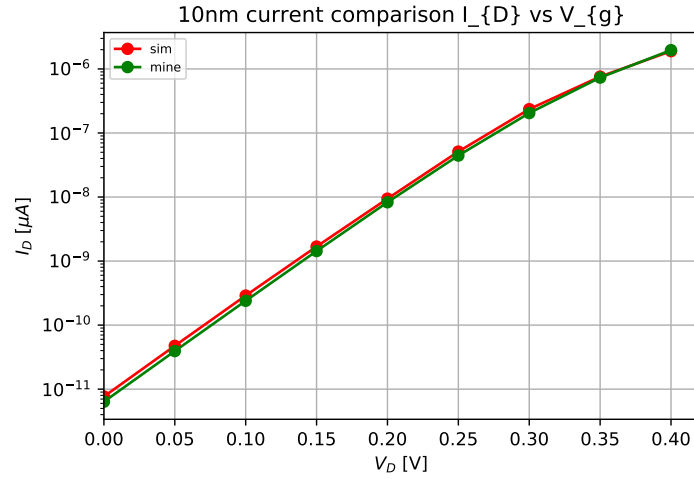


Figure 2.12: Current voltage curve for a 3nm x 3nm Silicon body cross-section and 10 nm channel length

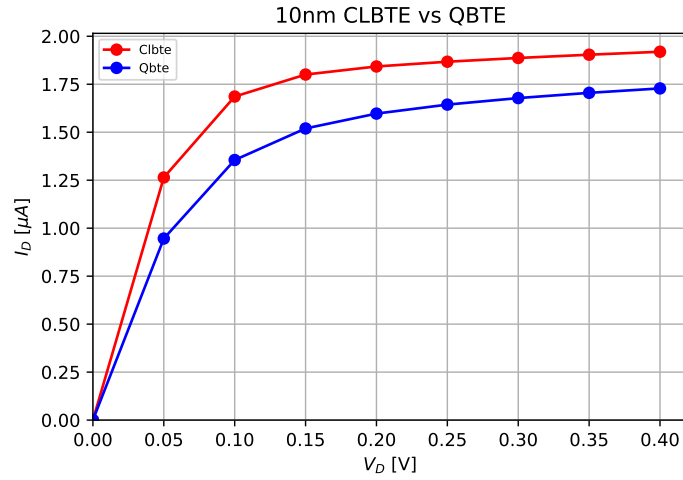


Figure 2.13: Current vs drain voltage curve of a 10 nm channel length for clbte and qbte

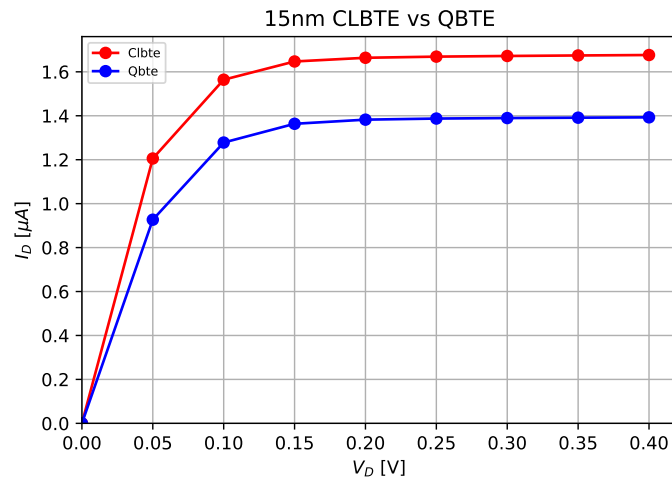


Figure 2.14: Current vs drain voltage curve of a 15 nm channel length for clbte and qbte

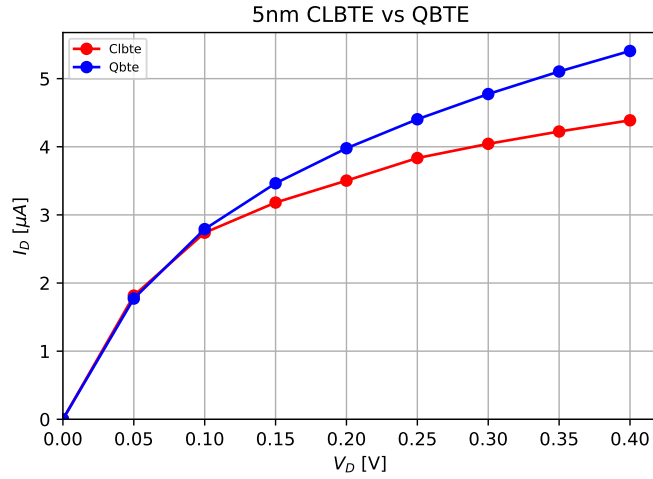


Figure 2.15: Current vs drain voltage curve of a 5 nm channel length for clbte and qbte

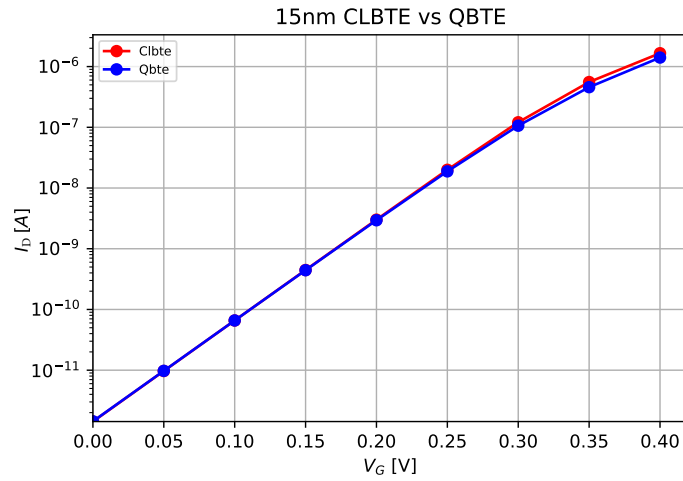


Figure 2.16: Current vs gate voltage curve of a 15 nm channel length for clbte and qbte

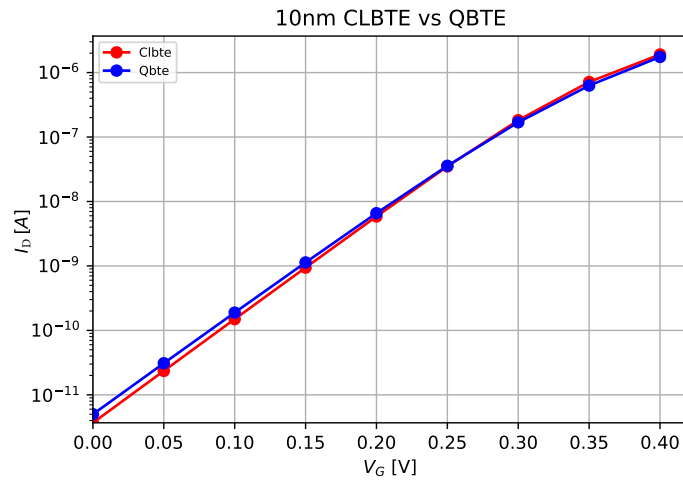


Figure 2.17: Current vs gate voltage curve of a 10 nm channel length for clbte and qbte

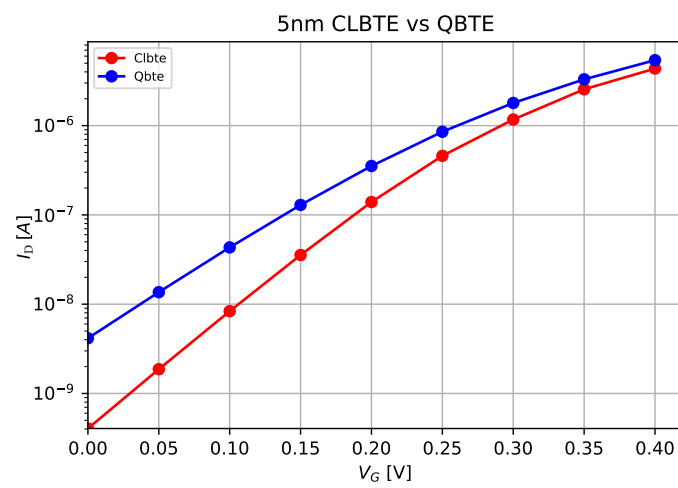


Figure 2.18: Current vs gate voltage curve of a 5 nm channel length for clbte and qbte

CHAPTER 3

Diffusive Transport

Diffusive transport is a scattering dominant and long channel phenomena. Scattering leads to loss in momentum and energy of the electrons. The performance of the device in this case is lower than the ballistic case because current is lower due to scattering. It implies an increase in channel resistance, increase in drain saturation voltage and an increase in output conductance. In a semiconductor, scattering can be due to various factors like electron interaction with impurities, electrons scattered by surface roughness, electron-phonon interaction, Coloumbic interaction, etc

In the simulation tool, diffusive transport is modelled semi-classically through drift-diffusion transport and quantum mechanically through Buttiker's probe method.

3.1 Drift-Diffusion Transport

Drift-Diffusion transport is a semi-classical transport mechanism, therefore, electrons are treated as particles. It is the solution to the Boltzmann Transport equation in the diffusive limit. Unlike the ballistic transport, even the electrons below the source-channel barrier can also go from the source end to the drain end.

Now, the current in a scattering dominant phenomena is lower than that in the ballistic case because the number of electrons reaching the drain is lesser as some of them get back-scattered into the source contact. In addition, electrons that reach the drain end have lower speed due to scattering in the channel. Most of the back-scattering takes place in the low field region near the source channel barrier-'the bottle neck'. Once an electron crosses the 'bottle neck' and reaches near the high field drain region the probability of back-scattering is minimal. In ballistic case, right moving electrons above the barrier were injected by the source while the left moving were injected by the drain, however, in case of scattering both the streams are mixed. Carrier density at the top of the channel is governed by MOS electrostatics which is solved using 3D Poisson's

equation. Since, the simulation tool is built for a thin SOI device, 1D drift-diffusion transport is solved in subbands obtained from the solution of 2D Schrodinger's equation. Scattering is basically included by modifying the value of electron mobility in the device.

Calculating the charge

Start with the drift-diffusion current equation

$$J_n = -qn\mu_n \frac{d\Phi}{dx} + qD_n \frac{dn}{dx} \quad (3.1)$$

where J_n is the electron current and n is the electron density but they are both unknowns so this equation can't be solved directly. Therefore, continuity equation is used to address this issue. The continuity equation is

$$\frac{\partial n}{\partial t} = \nabla(J_n/q) + G_n - \frac{\delta y}{\tau} \quad (3.2)$$

which for one dimensional transport along x direction without any generation or recombination reduces to

$$\frac{\partial n}{\partial t} = \frac{\partial}{\partial x}(J_n/q) \quad (3.3)$$

for steady-state solutions $\frac{\partial n}{\partial t} = 0$ which leads to

$$\frac{\partial}{\partial x}(J_n/q) = 0 \quad \text{or} \quad \frac{\partial}{\partial x}(J_n) = 0 \quad (3.4)$$

Now along the transport direction there are N_x grid points but using continuity equation results in only $N_x - 1$ equations. In order to solve this problem mid-point nodes are used.

Using Einstein's relation

$$\frac{D_n}{\mu_n} = \frac{k_B T}{q} \frac{n}{\frac{\partial n}{\partial \eta}} \quad \text{for degenerate semiconductors}$$

and

$$\frac{D_n}{\mu_n} = \frac{k_B T}{q} \quad \text{for non degenerate semiconductors} \quad (3.5)$$

where $\eta = (E - \mu)/(\frac{k_B T}{q})$

Equation 3.1 for one dimensional transport can be written as

$$J_n = k_B T \mu_n \left(-n \frac{d(\Phi/\frac{k_B T}{q})}{dx} + \frac{dn}{dx} \right) \quad (3.6)$$

or

$$J_n = k_B T \mu_n \left(-n \frac{d\phi}{dx} + \frac{dn}{dx} \right) \quad \text{where } \phi = \Phi/\frac{k_B T}{q} \quad (3.7)$$

Finally, applying FDM on equation 3.4 for midpoint nodes $i + 1/2$ and $i - 1/2$ gives

$$J_{i+1/2} = J_{i-1/2} \quad (3.8)$$

$$\begin{aligned} & k_B T \mu_{i+1/2} \left(-n_{i+1/2} \frac{\phi_{i+1} - \phi_i}{a} + \frac{n_{i+1} - n_i}{a} \right) \\ &= k_B T \mu_{i-1/2} \left(-n_{i-1/2} \frac{\phi_i - \phi_{i-1}}{a} + \frac{n_i - n_{i-1}}{a} \right) \end{aligned} \quad (3.9)$$

where a is the grid spacing along the transport direction

Now, in order to obtain the mobility and electron density at mid point nodes the first guess would be linear interpolation, resulting in

$$\begin{aligned} & \frac{\mu_{i-1} + \mu_i}{2} \left(-\frac{n_{i-1} + n_i}{2} \frac{\phi_i - \phi_{i-1}}{a} + \frac{n_i - n_{i-1}}{a} \right) \\ & \frac{\mu_i + \mu_{i+1}}{2} \left(-\frac{n_i + n_{i+1}}{2} \frac{\phi_{i+1} - \phi_i}{a} + \frac{n_{i+1} - n_i}{a} \right) \end{aligned} \quad (3.10)$$

Rearranging the terms gives

$$\begin{aligned} & (\phi_{i+1} - \phi_i - 2)n_{i+1} + \left(\frac{\mu_i + \mu_{i-1}}{\mu_i + \mu_{i+1}} (\phi_i - \phi_{i-1} - 2) + (\phi_{i+1} - \phi_i + 2) \right) n_i \\ & + \left(\frac{\mu_i + \mu_{i-1}}{\mu_i + \mu_{i+1}} n_{i-1} \right) (\phi_i - \phi_{i-1} + 2) = 0 \end{aligned} \quad (3.11)$$

But if the above equation is satisfied and both

$$\phi_{i+1} - \phi_i - 2 > 0 \text{ and } \phi_i - \phi_{i-1} - 2 > 0$$

or

$$\Phi_{i+1} - \Phi_{i-1} > 4 \frac{k_B T}{q}$$

then it implies that one or more of the electron density term in the equation becomes negative, but electron density being a physical quantity can't be negative. Therefore, if potential of two alternate nodes differ by $4k_B T/q$ an instability occurs. This usually happens at source(drain)-channel interface under high V_g and low V_d [12]. One way to avoid the instability is the use of finer grid near source or drain-channel interface but it results in more memory usage, therefore, Scharfetter and Gummel scheme[20][12] is employed in the simulator to bypass the issue.

It is known that potential can take both positive and negative values, therefore, for electron density to be positive always express it as $n = u e^\phi$ where u is a positive unknown function and ϕ is the potential.

Equation 3.10 was obtained from equation 3.9 by linear interpolation of mobility and electron density. Now, however, only mobility is linearly interpolated since it doesn't change abruptly while electron density and potential are no longer interpolated.

Therefore,

$$J_{i+1/2} = k_B T \frac{\mu_i + \mu_{i+1}}{2} \left(-n_{i+1/2} \frac{d\phi_{i+1/2}}{dx} + \frac{dn_{i+1/2}}{dx} \right) \quad (3.12)$$

$$J_{i-1/2} = k_B T \frac{\mu_i + \mu_{i-1}}{2} \left(-n_{i-1/2} \frac{d\phi_{i-1/2}}{dx} + \frac{dn_{i-1/2}}{dx} \right) \quad (3.13)$$

Substituting $n(x) = u(x)e^\phi$ in the equation(3.12) results in

$$J_{i+1/2} = k_B T \frac{\mu_i + \mu_{i+1}}{2} e^\phi \frac{du}{dx} \quad (3.14)$$

Now multiplying both sides by $e^{-\phi}$ and integrating between i and $i + 1$ gives

$$\int_i^{i+1} e^{-\phi} J_{i+1/2} dx = \int_i^{i+1} k_B T \frac{\mu_i + \mu_{i+1}}{2} \frac{du}{dx} dx \quad (3.15)$$

The continuity equation states that current is same everywhere in a subband along

the transport direction, therefore, it can be taken out of the integral and the LHS of equation 3.15 after considering a linear variation of $\phi(x)$ between i and $i+1$, integrating and substituting the limits becomes

$$\begin{aligned} \int_i^{i+1} e^{-\phi} J_{i+1/2} dx &= J_{i+1/2} \int_i^{i+1} \exp(-\phi_i(x_i) - \frac{\phi_{i+1}(x_{i+1}) - \phi_i(x_i)}{a}(x - x_i)) dx \\ &= -J_{i+1/2} \frac{a}{\phi_{i+1} - \phi_i} (e^{-\phi_{i+1}} - e^{-\phi_i}) \end{aligned} \quad (3.16)$$

The RHS of equation 3.15 on integration and substitution of limit becomes

$$\begin{aligned} \int_i^{i+1} k_B T \frac{\mu_i + \mu_{i+1}}{2} \frac{du}{dx} dx &= k_B T \frac{\mu_i + \mu_{i+1}}{2} (u_{i+1} - u_i) \\ &= k_B T \frac{\mu_i + \mu_{i+1}}{2} (n_{i+1} e^{-\phi_{i+1}} - n_i e^{-\phi_i}) \end{aligned} \quad (3.17)$$

Finally, equating equation 3.16 and 3.17 results in

$$J_{i+1/2} = \frac{k_B T}{2a} (\mu_i + \mu_{i+1}) \frac{\phi_{i+1} - \phi_i}{e^{\phi_{i+1} - \phi_i} - 1} (n_{i+1} - n_i e^{\phi_{i+1} - \phi_i}) \quad (3.18)$$

Let $B(\phi_{i+1} - \phi_i) = \frac{\phi_{i+1} - \phi_i}{e^{\phi_{i+1} - \phi_i} - 1}$

Similar to equation 3.18 an equation can be written for $J_{i-1/2}$ and then equated for continuity to get

$$\begin{aligned} &(\mu_i + \mu_{i-1}) B(\phi_i - \phi_{i-1}) e^{\phi_i - \phi_{i-1}} n_{i-1} \\ &- ((\mu_i + \mu_{i-1}) B(\phi_i - \phi_{i-1}) + (\mu_i + \mu_{i+1}) B(\phi_{i+1} - \phi_i) e^{\phi_{i+1} - \phi_i}) n_i \\ &+ (\mu_i + \mu_{i+1}) B(\phi_{i+1} - \phi_i) e^{\phi_{i+1} - \phi_i} n_{i+1} = 0 \end{aligned}$$

The above equation is implemented directly in the simulator. The Scharfetter and Gummel scheme is deployed only in the case of high field, otherwise, the conventional method of linear interpolation of electron density and mobility is continued. Everything discussed so far was done for non-degenerate semiconductors, for degenerate semiconductors, Einstein relation must be carefully used.

In addition to this, the electron density in subband m at source and drain ends de-

pend on the respective Fermi distribution and are defined as

$$n_s^m = 2 \int_0^\infty \frac{1}{\pi \hbar} \sqrt{\frac{m_x^*}{2E}} \frac{1}{1 + e^{\frac{E_i + E - \mu_s}{kT}}} dE \quad (3.19)$$

$$= \frac{1}{\hbar} \sqrt{\frac{2m_x^*}{\pi}} \mathfrak{S}_{-1/2} \left(-\frac{U_s + V_s}{kT/q} \right) \quad (3.20)$$

$$n_d^m = 2 \int_0^\infty \frac{1}{\pi \hbar} \sqrt{\frac{m_x^*}{2E}} \frac{1}{1 + e^{\frac{E_i + E - \mu_d}{kT}}} dE$$

$$= \frac{1}{\hbar} \sqrt{\frac{2m_x^*}{\pi}} \mathfrak{S}_{-1/2} \left(-\frac{U_d + V_d}{kT/q} \right) \quad (3.21)$$

A factor of 2 is included for spin degeneracy. In order to get the final charge, sum over all the subbands and valleys (in this case valley degeneracy of 2).

Calculating the current

Once the charge and Poisson's equation converge to a final potential profile and result in a subband, current can then be conveniently calculated using equation 3.12 and because of continuity current anywhere in the device is same.

3.2 Quantum Dissipative Transport

To accurately model nanoscale devices, a quantum mechanical treatment is necessary because it considers the effects of tunneling, interference and scattering. The quantum ballistic model is valid only in 'phase coherent limit' i.e. when the Schrodinger's equation gives a deterministic evolution of amplitude and phase of the wave function $\Psi_n(\vec{r})$. In general, quantum mechanical wave functions evolve phase coherently only in presence of rigid potentials like the electrostatic potential[11]. When electron waves encounter scatterers that have internal degree of freedom like phonons, they lose phase coherence information that can't be retrieved. This phenomenon becomes significant for device dimensions comparable to the scattering length of phonons and other such mechanisms, hence it should be carefully incorporated.

Scattering in quantum mechanical domain results in the loss in momentum and/(or)

energy as well the quantum mechanical phase. Change in momentum only corresponds to elastic scattering while change in both momentum and energy corresponds to inelastic scattering. As discussed in section 2.3.2 on Quantum ballistic transport, the wave function in the active device region has contributions from source Ψ_D^s , drain Ψ_D^d as well as from localized states Ψ_D^{loc} because of scattering.

In order to get the charge distribution in the device, the three dimensional Schrodinger's equation is solved as a combination of 2D Schrodinger's equation in a cross-section to incorporate confinement effects and 1D transport in the subbands obtained from the 2D equation. To incorporate all the effects efficiently and accurately, the 1D transport is treated through the NEGF approach . In the simulator developed as part of this work, uncoupled mode space approach is preferred for computational simplicity. Starting with equation(2.15) and then considering the wave function to be predominantly present in the silicon region leads to

$$-\frac{\hbar^2}{2}a_{mm}(x)\frac{\partial^2}{\partial x^2}\varphi^m(x) + E_{sub}^m\varphi^m(x) = E\varphi^m(x) \quad (3.22)$$

which describes each element of the device Hamiltonian H but doesn't include it's interaction with contacts. To consider the effect of contacts (discussed in ballistic transport in the previous chapter) and scattering, 'self energy' concept is used. The Green's function employed to address the modelling problem is

$$G^m(E) = [EI - H - \Sigma_s^m(E) - \Sigma_1^m(E) - \Sigma_2^m(E)]^{-1} \quad (3.23)$$

where H is $N_x \times N_x$ diagonal matrix whose each element are given by equation 3.23. The contact self-energy terms are same as in equation 2.35 and 2.36. The next step is to describe the scattering self-energy function, which varies depending on the kind of scattering phenomena considered.

In this work a simple phenomenological approach namely, "Buttiker's Probe" method [5] [13] [21] is followed to incorporate scattering. It is similar to the drift-diffusion method as it is an approximate approach as well. In order to consider scattering in detail, electron-phonon interaction, scattering due to surface roughness, etc must be addressed rigorously.

Buttiker probes are virtual probes assumed to be attached to the lattice in the trans-

port direction. They are supposed to absorb electrons, change their momenta and/or energies and then release them back into the channel without any change in the number of electrons (number of electrons change only at the source and drain contacts). Since these probes act as virtual reservoirs they are each represented by an electro-chemical potential μ_i , which is obtained after imposing current continuity at the probes.

Figure 3.1 shows probes attached to a mode (subband) in the transport direction. The coupling between the probes and any subband m is given by Δ_m^i , the coupling energy, where i is the position of the probe along the transport direction. $\Delta_m^i = 0$ implies no coupling between probes and the subbands, hence no scattering into the probe i.e. ballistic transport. Higher the value of Δ_m^i , higher is the scattering in the device.

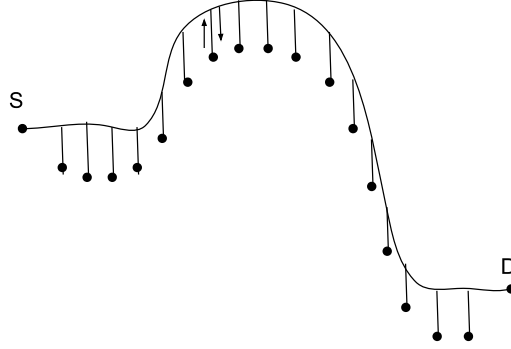


Figure 3.1: Representation of Buttiker's probes attached to a mode. The arrows show current flowing in and out of the probe

The Buttiker probe coupling strength Δ_m^i for single subband occupancy is defined as

$$\frac{\Delta_m^i}{t_m} = \frac{2a}{\lambda} \quad (3.24)$$

where $t_m = -\frac{\hbar^2}{2}a_{mm}$ is the coupling between adjacent lattice nodes as defined in section 2.3.2, a_{mm} is defined in equation 2.33. λ is the electron mean-free path and is related to the diffusivity as $D = v_T \frac{\lambda}{2}$ [13], hence to the low-field mobility μ as $\lambda = \frac{2k_B T}{qv_T} \mu \left(\frac{\mathfrak{S}_{-1/2}(\eta^i)}{\mathfrak{S}_{-3/2}(\eta^i)} \right)$ for a 1D conductor, v_T is the thermal velocity of degenerate car-

riers and is defined as $v_T = \sqrt{\frac{2k_B T}{\pi m^*}} \left(\frac{\Im_0(\eta^i)}{\Im_{-1/2}(\eta^i)} \right)$. This finally leads to the relation used in the simulator

$$\lambda = \left(\frac{2\mu}{\sqrt{\frac{2k_B T}{\pi m_x^*}}} \frac{k_B T}{q} \right) \frac{(\Im_{-1/2}(\eta^i))^2}{\Im_{-3/2}(\eta^i) \Im_0(\eta^i)} \quad (3.25)$$

where $\eta^i = \frac{\mu^i - E_m^i}{k_B T/q}$ is a position and energy dependent term. This makes λ position dependent and hence Δ_m^i position and energy dependent.

When multiple subbands are considered, an average value of λ is used which is obtained by estimating an average value of the thermal velocity considering all the subbands. In the device under consideration, the channel region is undoped hence carrier mobility should be higher, however, since it is a thin device the mobility is reduced due to surface roughness. It is therefore assumed that both the effects compensate each other. It is reported that electrons have a mobility $\sim 200 \text{ cm}^2/\text{Vs}$ for a charge density of $\sim 10^{13} \text{ cm}^{-2}$. The source and drain are doped highly to 10^{20} cm^{-3} and using a doping dependent model results in mobility of $\sim 55 \text{ cm}^2/\text{Vs}$ [21]. These are the values used in the simulator for this model.

Now, the scattering self-energy depends on the interaction of the device with the probes and the effect these probes have on the coupling between two adjacent nodes of the device (the device Hamiltonian). For a mode m , at any node i , it is defined as

$$\Sigma_s^m(E) = -\Delta_m^i (\exp(jk_{m,i}a) - 1) \quad (3.26)$$

where a is the spacing between successive nodes and $j = \sqrt{-1}$.

Therefore, self-energy in the device is $\Sigma^m = \Sigma_s^m + \Sigma_1^m + \Sigma_2^m$ has contribution from the scattering term, and both the contacts.

$$\Sigma^m = \begin{bmatrix} -t_m e^{jk_{m,1}a} & 0 & \dots & \dots & 0 \\ 0 & -\Delta_m^2 (e^{jk_{m,2}a} - 1) & 0 & \ddots & \vdots \\ \vdots & \ddots & \ddots & \ddots & \vdots \\ \vdots & \ddots & 0 & -\Delta_m^{N_x-1} (e^{jk_{m,N_x-1}a} - 1) & 0 \\ 0 & \dots & \dots & 0 & -t_m e^{jk_{m,N_x}a} \end{bmatrix}$$

Now that $\Sigma^m(E)$ and H are known, the Green's function can be evaluated using equation

3.23 which can then be used to evaluate the charge density and the current in the device.

The spectral density function due to source, drain and all the probes at any node i can be evaluated as

$$A_i^m(E) = G^m(E)\Gamma_i^m(E)G^{m\dagger}(E) \quad (3.27)$$

where Γ_i represents the electron exchange rate between the device and the reservoirs, is a $N_x \times N_x$ matrix and is given by

$$\Gamma_i^m[p, q] = j \left[\Sigma_i^m[p, q] - \Sigma_i^{m\dagger}[p, q] \right] \delta_{p,i} \delta_{q,i}, (p, q = 1, 2, 3, \dots, N_x) \quad (3.28)$$

The local density of states injected by reservoir i is given as

$$D_i^m[p] = \frac{1}{2\pi a} A_i^m[p, p] \quad (3.29)$$

and the 1D electron density for mode m has contribution from all reservoirs i and a spin degeneracy factor of 2, therefore, can be calculated as

$$n_{1D}^m = 2 \sum_{i=1}^{N_x} \int_{-\infty}^{\infty} D_i^m f(\mu_i, E) dE \quad (3.30)$$

In order to calculate the net 1D electron density, a sum over all subbands and valleys (valley degeneracy of 2) must be performed. Finally, the 3D electron density is evaluated as

$$n_{3D} = 2 \sum_{m=1}^M n_{1D}^m |\xi(y, z, x)|^2 / (dy * dz) \quad (3.31)$$

The transmission coefficient between any two reservoirs i and r is evaluated as

$$T_{i \leftrightarrow r}^m(E) = \text{trace} [\Gamma_i^m(E) G^m(E) \Gamma_r^m(E) G^{m\dagger}(E)] \quad (3.32)$$

The net current density at any reservoir considering all subbands and valleys i is

$$I_i = \frac{4q}{2\pi\hbar} \sum_{m=1}^M \sum_{r=1}^{N_x} \int_{-\infty}^{\infty} T_{i \leftrightarrow r}^m(E) (f(\mu_i, E) - f(\mu_r, E)) dE \quad (3.33)$$

Now, the Fermi level of the source and drain contact depend on the bias applied to them but that of the virtual reservoirs must be found using current continuity at these

nodes. So $I_i = 0$ for $i = 2, 3, 4, \dots, N_x - 1$.

$$\frac{2q}{\pi\hbar} \sum_{m=1}^M \sum_{r=1}^{N_x} \int_{-\infty}^{\infty} T_{i \leftrightarrow r}^m(E) (f(\mu_i, E) - f(\mu_r, E)) dE = 0 \quad (3.34)$$

The above is a set of non-linear equations which is solved iteratively using Newton-Raphson's method. The diagonal elements of the Jacobian involved are given as

$$J^{ii} = \frac{\partial I_i}{\partial \mu_i} = \frac{2q}{\pi\hbar} \sum_m \left[\frac{\partial f}{\partial \mu_i} \sum_{r, r \neq i} T_{i \leftrightarrow r}^m \right] dE \quad (3.35)$$

while the off-diagonal elements are given as

$$J^{ir} = \frac{\partial I_i}{\partial \mu_r} = -\frac{2q}{\pi\hbar} \sum_m \left[\sum_{r, r \neq i} \frac{\partial f}{\partial \mu_r} T_{i \leftrightarrow r}^m \right] dE \quad (3.36)$$

The solution to the Fermi-level at the reservoirs $i = 2, 3, \dots, N_x - 1$ is then obtained using

$$\Delta\mu = -J^{-1}I \quad (3.37)$$

$$\mu^{new} = \mu^{old} + \Delta\mu \quad (3.38)$$

3.3 Results and Discussions

In this chapter two types of dissipative transport are described- the semi-classical drift-diffusion and the quantum dissipative Buttiker's probe model. In this section, the mentioned dissipative transports are compared with their ballistic analogues to illustrate the degradation in current due to scattering.

For all the simulations involving drift-diffusion transport, the mobility value is taken as $\mu = 500 \text{ cm}^2 / \text{V} \cdot \text{s}$

Figures 3.2 and 3.3 show a comparison between the semi-classical ballistic and drift-diffusion transport. The 15nm channel shows comparatively a larger degradation in current from the ballistic case due to more scattering. The device considered here has a silicon cross-section of $3 \text{ nm} \times 3 \text{ nm}$.

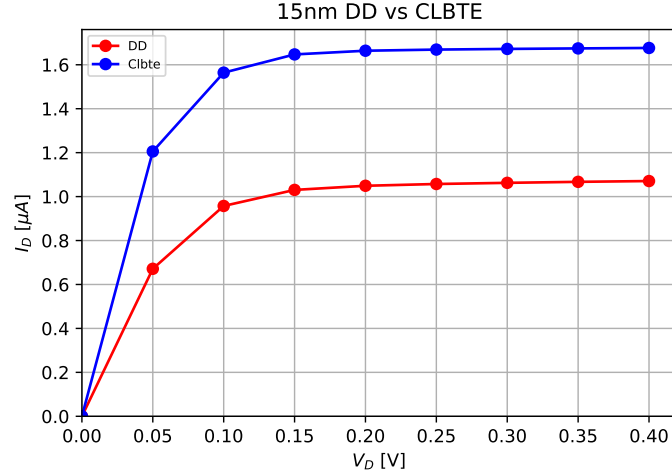


Figure 3.2: Current vs drain voltage curve of a 15 nm channel length for clbte and dd

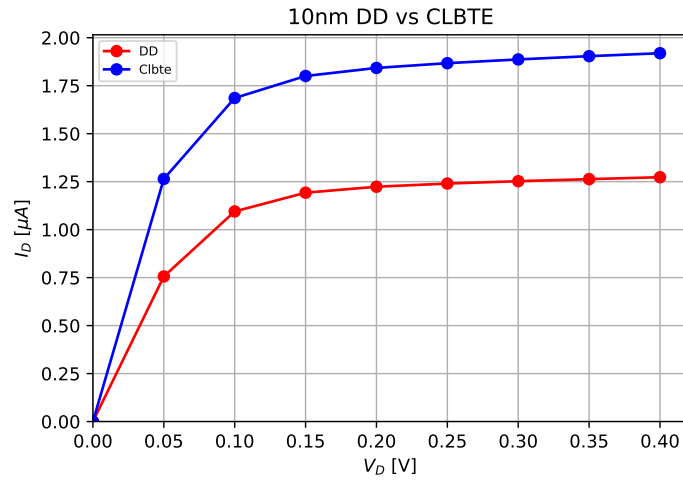


Figure 3.3: Current vs drain voltage curve of a 10 nm channel length for clbte and dd

The value of mobility used in the simulation of the quantum dissipative model is $200\text{cm}^2/Vs$ in the channel and $55\text{cm}^2/Vs$ in the source and drain extension regions.

Figure 3.4, 3.5 and 3.6 show a comparison between the ballistic and dissipative transport in the quantum domain. It can be easily seen that scattering is maximum in the long channel 15nm device and is less prominent in 5nm device indicating a trend towards the ballistic nature of transport. Figure 3.7 shows a comparison between the drain current vs. the gate voltage for a 15nm long channel and indicates an obvious decrease in the value of current from ballistic to dissipative for all bias. Even for 5nm channel length as in figure 3.8, the current involving scattering is much lower than the ballistic case

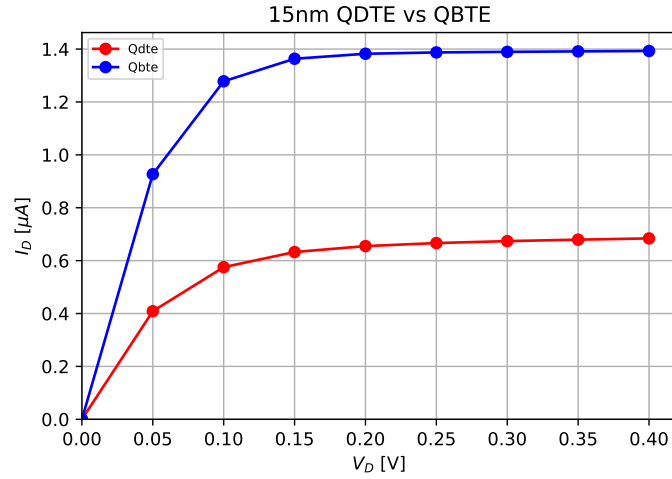


Figure 3.4: Current vs drain voltage curve of a 15 nm channel length for qbte and qdte

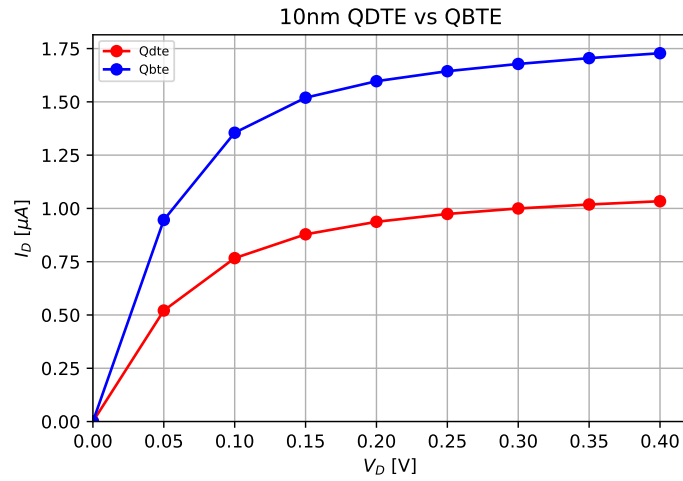


Figure 3.5: Current vs drain voltage curve of a 10 nm channel length for qbte and qdte

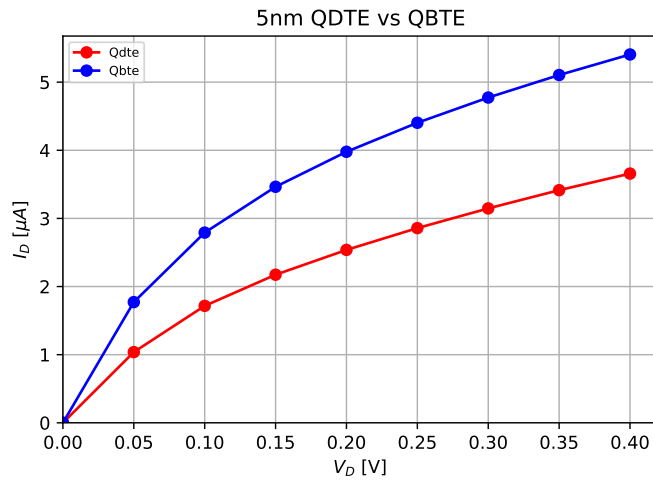


Figure 3.6: Current vs drain voltage curve of a 5 nm channel length for qbte and qdte

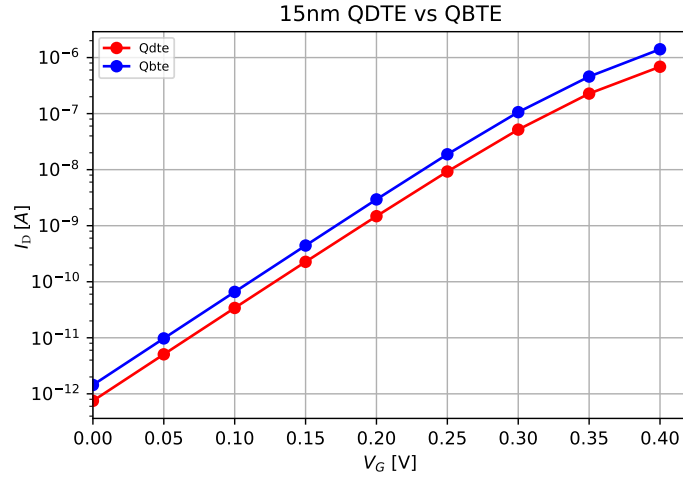


Figure 3.7: Current vs gate voltage curve of a 15 nm channel length for qbte and qdte

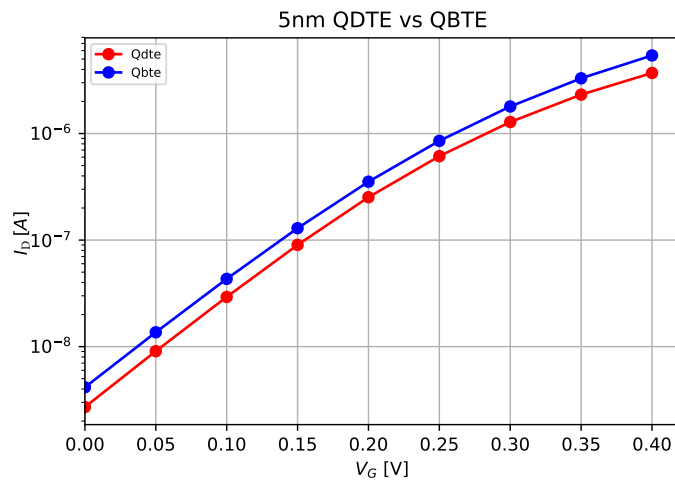


Figure 3.8: Current vs gate voltage curve of a 5 nm channel length for qbte and qdte

CHAPTER 4

Self Heating Effects in a Silicon Nanowire

In bulk transistors, heat generated in the channel could be easily removed through the silicon body which has a high thermal conductivity, so self heating effects were not so prominent. However, when the technology moved to SOI substrates, the buried silicon dioxide which has about 100 times lower thermal conductivity than bulk silicon posed problems in heat removal. The thermal conductivity of nanowires and the surrounding oxide layers is even lower when compared to the bulk or SOI transistors. This leads to prominent self-heating effects and localized hot spots which strongly affect the electrical characteristics. Because of the small dimension of nanowires, it is difficult to experimentally determine the temperature inside the device; numerical simulations come to aid at this juncture.

In order to model the thermal effects effectively there are two important issues - the heat generation mechanism and the heat transfer. Heat generation in any device is due to the scattering of the charge carriers (electrons in this case) by various mechanisms like electron-impurity scattering, electron-phonon interaction, etc. But the important part of the problem is the heat transfer from the region of generation to the other parts of the device. Just like the electrical transport, heat transport can be modelled semi-classically or quantum mechanically in the atomistic domain. The Arizona state university group has developed a particle based Monte-Carlo simulator using the energy balance equations derived from the Boltzmann transport equation for electrons and acoustic and optical phonons [22] [23] [24] [25] [26]. However, in the nanoscale limit this semi-classical treatment does not consider quantum effects, therefore the group in ETH has modelled a coupled electron-phonon thermal transport in the atomistic domain using the NEGF framework and have conducted various studies [27][28][29][30][31].

Both the mentioned approaches to treatment of thermal effects in transistors are well established and valid in certain limits but they are both computationally expensive. Therefore, as part of this thesis a numerically simple approach viz. the Fourier's law is used to model heat transport in the device. Fourier's law is a phenomenological

approach and valid mostly in the macroscopic domain. Several research groups have published questioning its validity in the nanoregime, like [32]. But a recent study[33] states that Fourier's law can be used in nanodomain if appropriate corrections are made to the temperature at the contacts.

4.1 Fourier's Law

For any temperature gradient within a solid, thermal energy flows from high temperature to low temperature. This phenomenon of heat conduction is described by Fourier's law

$$q = -\kappa \Delta T \quad (4.1)$$

where q is the heat flux vector, κ is the thermal conductivity and T is the local temperature.

Now for steady-state problems, the divergence of the heat flux vector can be written as

$$\nabla q = -\nabla (\kappa \nabla T) \quad (4.2)$$

where the divergence of the heat flux vector is related to the local heat generation in the device. In this case, heat is generated when electrons lose energy due to scattering which is most commonly modelled as the Joule heating. However, Joule heating considers only the electrons flowing at the conduction band minima and any effect of "hot-electrons" is not taken into account [34]. Therefore, the heat generation term which is basically the local power density in the device is given by

$$P = -\nabla (J_E) \quad (4.3)$$

where J_E is the energy current density and is given by

$$J_E(y, z; x) = \left[\int \frac{1}{q} E I_i(E) dE \right] |\xi(y, z; x)|^2 \quad (4.4)$$

where $I_i(E)$ is the energy dependent current at any node i along the transport direction.

The final expression incorporated in the simulations is

$$P = -\nabla \cdot J_{E_k} + \vec{\mathcal{E}} \cdot \tilde{\mathbf{J}} \quad (4.5)$$

where $\nabla \cdot J_{E_k}$ is the change in the kinetic energy part of the current density of the electron ensemble, $\vec{\mathcal{E}}$ is the local electric field in the device, and $\tilde{\mathbf{J}}$ is the current density.

The solution of the equation can't be obtained unless proper boundary conditions are incorporated. The device interacts with the ambient through

Metallic Gate boundary: In the thermal simulation considered in this work, these gates are considered both floating or as heat sinks and hence lead to different results. Floating boundary conditions (Neumann) imply no heat transfer to the ambient. For heat to flow through the gates to some heat sinks they are usually connected through a thermal resistance to a lower temperature node. In the simulations however, they are connected directly to a $300K$ heat sink.

Semiconductor/oxide metallic source/drain interface: Source and drain are considered as heat sinks always and are at $300K$ for all simulations.

Oxide/ambient interface: No heat is supposed to flow through these interfaces as radiation is not considered.

Similar to the method of solving the Poisson's equation, apply the control volume method to equation(4.2) to get

$$\begin{aligned} f_\alpha = & \frac{1}{4} \left[-T_{m,n,p} \left(\frac{\Delta y \Delta z}{\Delta x} + \frac{\Delta x \Delta z}{\Delta y} + \frac{\Delta x \Delta y}{\Delta z} \right) \left(\sum_{i=1}^8 \kappa_i \right) + \right. \\ & T_{m+1,n,p} (\kappa_1 + \kappa_4 + \kappa_5 + \kappa_8) \frac{\Delta y \Delta z}{\Delta x} + T_{m-1,n,p} (\kappa_2 + \kappa_3 + \kappa_6 + \kappa_7) \frac{\Delta y \Delta z}{\Delta x} + \\ & T_{m,n+1,p} (\kappa_1 + \kappa_2 + \kappa_5 + \kappa_6) \frac{\Delta x \Delta z}{\Delta y} + T_{m,n-1,p} (\kappa_3 + \kappa_4 + \kappa_7 + \kappa_8) \frac{\Delta x \Delta z}{\Delta y} + \\ & \left. T_{m,n,p+1} (\kappa_1 + \kappa_2 + \kappa_3 + \kappa_4) \frac{\Delta x \Delta y}{\Delta z} + T_{m,n,p-1} (\kappa_5 + \kappa_6 + \kappa_7 + \kappa_8) \frac{\Delta x \Delta y}{\Delta z} \right] \\ & - (\Delta x \Delta y \Delta z) P_{n,m,p} \end{aligned} \quad (4.6)$$

This non-linear equation is solved iteratively using Newton's method to get a new

temperature profile till a convergence is achieved.

4.2 Thermal Conductivity

Before proceeding to the results obtained from the thermal simulations, it is essential to look at the thermal conductivity of Silicon nanowires. When compared to the bulk counterpart the thermal conductivity of thin films decreases due to the phonon boundary scattering, change in phonon dispersion relation due to confinement and the quantization of phonon transport[35]. For thinner wires the boundary scattering is even more, hence the thermal conductivity decreases further leading to lower thermal conduction. For the sake of simplicity all the simulations were done for silicon thermal conductivity of 5 W/(mK) and oxide thermal conductivity of 0.05 W/(mK). The main objective here is to point the sanity of the method used. The value of thermal conductivity can be appropriately used.

4.3 Results and discussion

So far all the simulations were done for a fixed temperature of 300K i.e isothermal simulations. Now, because of carrier scattering temperature of the device increases and therefore affects the mobility and concentration of the charge carriers. The characteristics of the device are expected to degrade.

Figure 4.1, 4.2, 4.3 show the current vs. drain voltage characteristics under isothermal and thermal cases with different boundary conditions. It is observed that the degradation is not much for the $V_g = 0.4V$ for different V_d but at higher voltages the electrical characteristics are expected to degrade more. When source, drain and gates are all considered heat sinks, heat removal is more effective as compared to when only source and drain are considered heat sinks. The degradation is more in the latter case as can be seen in figure 4.4

When gate is considered a heat sink along with source and drain the temperature along the transport direction for different V_d is shown in figure 4.5, while if only source and drain are considered as sinks then the temperature variation with x for different V_D

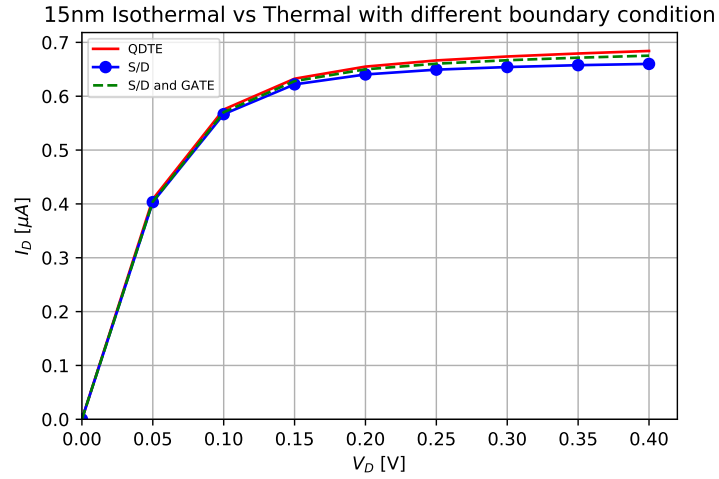


Figure 4.1: Current vs drain voltage curve of a 15 nm channel length for qbte and qdte

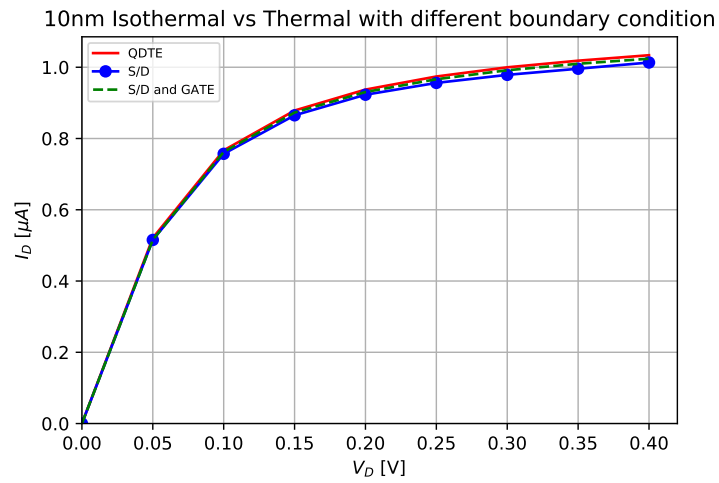


Figure 4.2: Current vs drain voltage curve of a 10 nm channel length for qbte and qdte

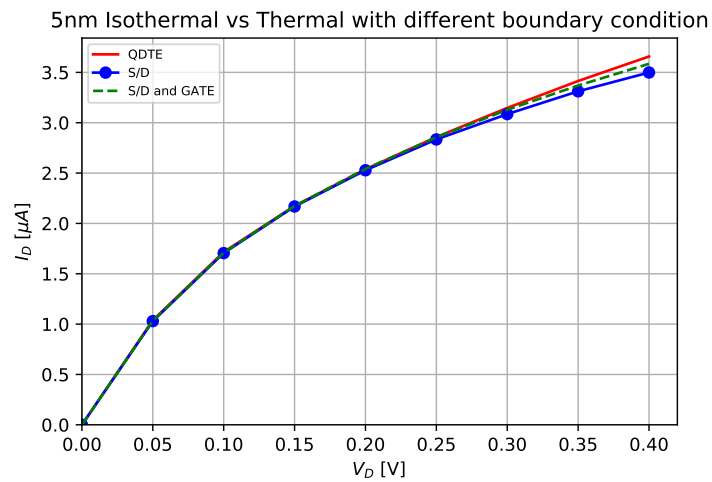


Figure 4.3: Current vs drain voltage curve of a 5 nm channel length for qbte and qdte

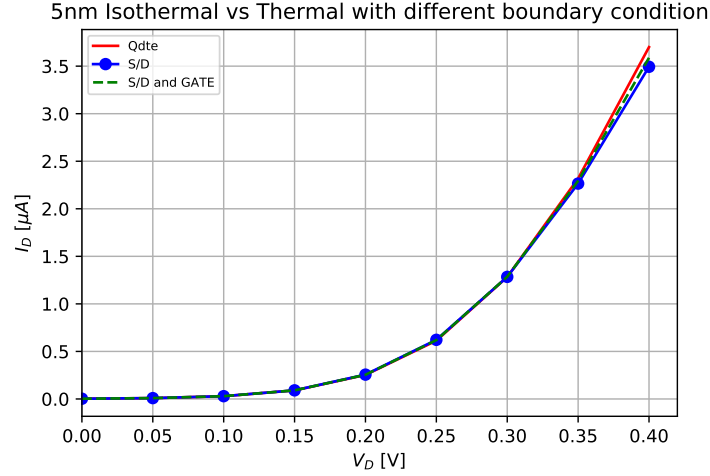


Figure 4.4: Current vs gate voltage curve of a 5 nm channel length for qbte and qdte

is shown in 4.6. If the gate is considered as heat sink along with source and drain, the net area for heat removal increases, therefore, the temperature rise is lower as compared to when only source and drain are considered as heat sinks.

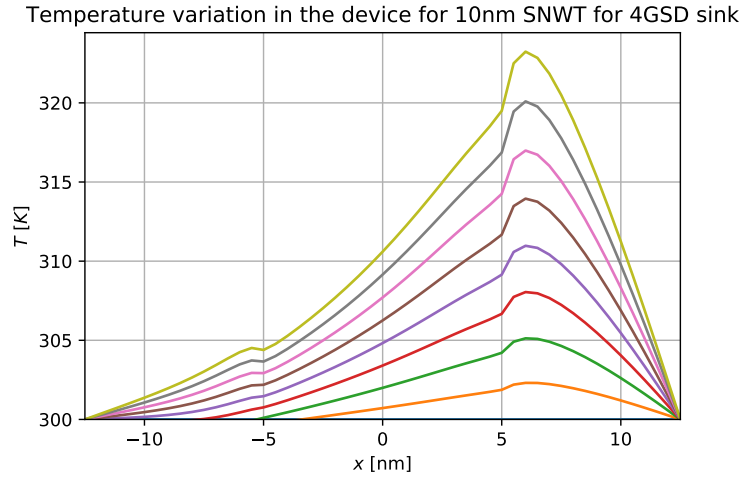


Figure 4.5: Temperature variation along the transport direction for different V_D when source, drain and gate are all heat sinks

With increase in the temperature in the device, the charge concentration increases but because of the increased scattering the mobility decreases which leads to a lower drain current.

Mobility model used in the simulator developed is Caughey-Thomas model and is given as

$$\mu_n = \mu_{low} + \frac{\mu_{min}(T/300)^{-2.3} - \mu_{low}}{1 + (N/N_{ref})^{-3.8}} \quad (4.7)$$

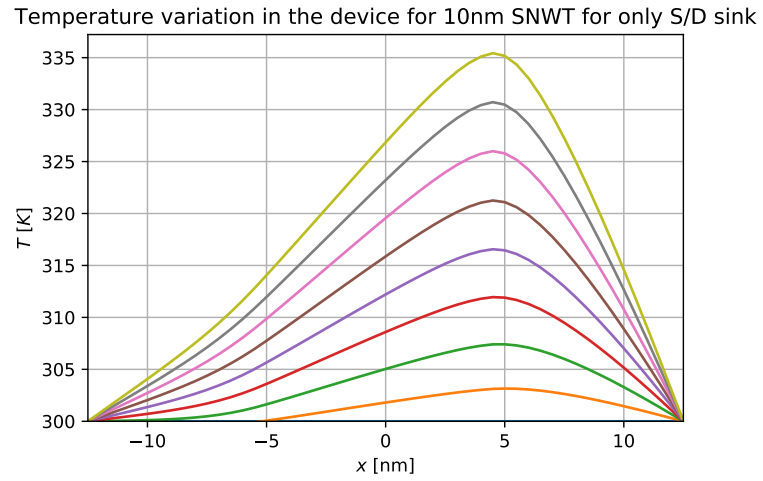


Figure 4.6: Temperature variation along the transport direction for different V_D when only source and drain are heat sinks

The final device characteristics are not as degraded as one would expect because the charge carriers are in the velocity overshoot region thereby compensating for the decrease in mobility.

CHAPTER 5

CONCLUSION

5.1 Summary

The thesis describes device physics and modelling of a SNWT both at the semi-classical and the quantum level based on effective mass approximation. The Poisson's equation describes the electrostatics in the device, and the Schrodinger's equation deals with the charge carrier transport and its distribution.

Schrodinger's equation was solved in mode-space, which transformed the 3D problem to a 2D confinement + 1D transport problem. This results in lower memory requirement, also the time required for simulation reduces drastically when compared to a real space approach.

Finite Difference Method(FDM) was used to discretize the equations involved. For the validity of the usage of bulk effective mass the lower limit of the thickness and width of the SNWT was fixed to 3nm while for the validity of the mode-space the upper limit was fixed to 5nm [11] [13]. The length of the channel was varied from 5nm to 15nm for various comparisons.

1D transport was addressed in chapters 2 and 3 both quantum mechanically using NEGF and semi-classically using BTE and a comparative study of both ballistic and dissipative transport was presented.

Finally, in chapter 4 using Fourier's law, self-heating in SNWT was analyzed and it was observed that the number of heat sinks determined the final device temperature and hence the device characteristics. More the number of heat sinks lower is the degradation in the final current.

5.2 Scope for future work

1) Scattering can be incorporated more rigorously through electron-phonon interaction model.

2) Instead of Finite Difference Method (FDM) a Finite Element Method (FEM) can be used in the development of the simulator. This will allow one to explore SNWT of different cross-section [12].

3) In this work, for the purpose of simplicity Fourier's law is employed for considering heat transport in the SNWT. However, for a more rigorous analysis electron-phonon interaction could be considered specifically either in the atomistic domain or the continuum domain.

4) The device is made with a Silicon substrate. A different material could be used as a substrate too and then the results could be analyzed.

REFERENCES

- [1] D. J. Frank, R. H. Dennard, E. Nowak, P. M. Solomon, Y. Taur, and H.-S. P. Wong, "Device scaling limits of si mosfets and their application dependencies," *Proceedings of the IEEE*, vol. 89, no. 3, pp. 259–288, 2001.
- [2] J.-P. Colinge, *Silicon-on-Insulator Technology: Materials to VLSI: Materials to Vlsi*. Springer Science & Business Media, 2004.
- [3] R. Courtland, "Transistors could stop shrinking in 2021," *IEEE Spectrum*, vol. 53, no. 9, pp. 9–11, 2016.
- [4] Y. Taur and T. H. Ning, *Fundamentals of modern VLSI devices*. Cambridge university press, 2013.
- [5] J. Wang, E. Polizzi, and M. Lundstrom, "A three-dimensional quantum simulation of silicon nanowire transistors with the effective-mass approximation," *Journal of Applied Physics*, vol. 96, no. 4, pp. 2192–2203, 2004.
- [6] E. Dastjerdy, R. Ghayour, and H. Sarvari, "3d quantum mechanical simulation of square nanowire mosfets by using negf method," *Central European Journal of Physics*, vol. 9, no. 2, pp. 472–481, 2011.
- [7] M. Shin, "Efficient simulation of silicon nanowire field effect transistors and their scaling behavior," *Journal of applied physics*, vol. 101, no. 2, p. 024510, 2007.
- [8] Y.-J. Ko, M. Shin, J. S. Ha, and K. W. Park, "Green-function calculations of coherent electron transport in a gated si nanowire," *ETRI journal*, vol. 22, no. 3, pp. 19–26, 2000.
- [9] G. Fiori and G. Iannaccone, "Three-dimensional simulation of one-dimensional transport in silicon nanowire transistors," *IEEE Transactions on Nanotechnology*, vol. 6, no. 5, pp. 524–529, 2007.
- [10] M. Bescond, N. Cavassilas, K. Kalna, K. Nehari, L. Raymond, J. Autran, M. Lanoo, and A. Asenov, "Ballistic transport in si, ge, and gaas nanowire mosfets," in *Electron Devices Meeting, 2005. IEDM Technical Digest. IEEE International*. IEEE, 2005, pp. 526–529.
- [11] M. Anantram, M. S. Lundstrom, and D. E. Nikonov, "Modeling of nanoscale devices," *Proceedings of the IEEE*, vol. 96, no. 9, pp. 1511–1550, 2008.
- [12] X. Wang, "Nanomos 4.0: A tool to explore ultimate silicon transistors and beyond," Ph.D. dissertation, Purdue University, 2010.
- [13] Z. Ren, "Nanoscale mosfets: Physics, simulation and design," Ph.D. dissertation, Purdue University, 2001.
- [14] R. Venugopal, Z. Ren, S. Datta, M. Lundstrom, and D. Jovanovic, "Simulating quantum transport in nanoscale transistors: Real versus mode-space approaches," *Journal of Applied Physics*, vol. 92, no. 7, pp. 3730–3739, 2002.

- [15] M. Lundstrom and Z. Ren, “Essential physics of carrier transport in nanoscale mosfets,” *IEEE Transactions on Electron Devices*, vol. 49, no. 1, pp. 133–141, 2002.
- [16] A. Rahman, J. Guo, S. Datta, and M. S. Lundstrom, “Theory of ballistic nanotransistors,” *IEEE Transactions on Electron Devices*, vol. 50, no. 9, pp. 1853–1864, 2003.
- [17] S. Datta, *Quantum transport: atom to transistor*. Cambridge University Press, 2005.
- [18] M. Paulsson, “Non equilibrium green’s functions for dummies: Introduction to the one particle negf equations,” *arXiv preprint cond-mat/0210519*, 2002.
- [19] M. Shin, “Multi-gate nanowire fet,” May 2007. [Online]. Available: <https://nanohub.org/resources/2704>
- [20] D. L. Scharfetter and H. K. Gummel, “Large-signal analysis of a silicon read diode oscillator,” *IEEE Transactions on electron devices*, vol. 16, no. 1, pp. 64–77, 1969.
- [21] R. Venugopal, M. Paulsson, S. Goasguen, S. Datta, and M. Lundstrom, “A simple quantum mechanical treatment of scattering in nanoscale transistors,” *Journal of Applied Physics*, vol. 93, no. 9, pp. 5613–5625, 2003.
- [22] K. Raleva, D. Vasileska, S. M. Goodnick, and M. Nedjalkov, “Modeling thermal effects in nanodevices,” *IEEE Transactions on Electron Devices*, vol. 55, no. 6, pp. 1306–1316, 2008.
- [23] D. Vasileska, K. Raleva, and S. M. Goodnick, “Self-heating effects in nanoscale fd soi devices: The role of the substrate, boundary conditions at various interfaces, and the dielectric material type for the box,” *IEEE Transactions on Electron Devices*, vol. 56, no. 12, pp. 3064–3071, 2009.
- [24] D. Vasileska, K. Raleva, and S. M. Goodnick, “Electrothermal studies of fd soi devices that utilize a new theoretical model for the temperature and thickness dependence of the thermal conductivity,” *IEEE Transactions on Electron Devices*, vol. 57, no. 3, pp. 726–728, 2010.
- [25] D. Vasileska, A. Hossain, and S. M. Goodnick, “The role of the source and drain contacts on self-heating effect in nanowire transistors,” *ECS Transactions*, vol. 31, no. 1, pp. 83–90, 2010.
- [26] D. Vasileska, “Self-heating in soi nano devices,” in *Nanotechnology Materials and Devices Conference (NMDC), 2010 IEEE*. IEEE, 2010, pp. 389–394.
- [27] R. Rhyner and M. Luisier, “Atomistic modeling of coupled electron-phonon transport in nanowire transistors,” *Physical Review B*, vol. 89, no. 23, p. 235311, 2014.
- [28] R. Rhyner and M. Luisier, “Influence of anharmonic phonon decay on self-heating in si nanowire transistors,” *Applied Physics Letters*, vol. 105, no. 6, p. 062113, 2014.
- [29] R. Rhyner and M. Luisier, “Self-heating effects in ultra-scaled si nanowire transistors,” in *Electron Devices Meeting (IEDM), 2013 IEEE International*. IEEE, 2013, pp. 32–1.

- [30] R. Rhyner and M. Luisier, “Minimizing self-heating and heat dissipation in ultra-scaled nanowire transistors,” *Nano letters*, vol. 16, no. 2, pp. 1022–1026, 2016.
- [31] R. Rhyner and M. Luisier, “Influence of thermal losses at the gate contact of si nanowire transistors: A phenomenological treatment in quantum transport theory,” *Applied Physics Letters*, vol. 110, no. 10, p. 103508, 2017.
- [32] N. Yang, G. Zhang, and B. Li, “Violation of fourier’s law and anomalous heat diffusion in silicon nanowires,” *Nano Today*, vol. 5, no. 2, pp. 85–90, 2010.
- [33] J. Kaiser, T. Feng, J. Maassen, X. Wang, X. Ruan, and M. Lundstrom, “Thermal transport at the nanoscale: A fourier’s law vs. phonon boltzmann equation study,” *Journal of Applied Physics*, vol. 121, no. 4, p. 044302, 2017.
- [34] R. Lake and S. Datta, “Energy balance and heat exchange in mesoscopic systems,” *Physical Review B*, vol. 46, no. 8, p. 4757, 1992.
- [35] D. Li, Y. Wu, P. Kim, L. Shi, P. Yang, and A. Majumdar, “Thermal conductivity of individual silicon nanowires,” *Applied Physics Letters*, vol. 83, no. 14, pp. 2934–2936, 2003.